An ISO[1] Far-Infrared Survey of Line and Continuum Emission for 227 Galaxies

James R. Brauher
Infrared Processing and Analysis Center, MS 100-22
California Institute of Technology,
Pasadena, CA 91125
jimby@ipac.caltech.edu

Received _____; Accepted _____

For Submission to the Astrophysical Journal Supplement

[1]Based on observations with ISO, an ESA project with instruments funded by ESA member states (especially the PI countries: France, Germany, the Netherlands, and the United Kingdom) with the participation of ISAS and NASA.

ABSTRACT

Far-infrared (FIR) line and continuum fluxes are presented for a sample of 227 (46 resolved, 181 unresolved) galaxies observed with the Long Wavelength Spectrometer (LWS) on the *Infrared Space Observatory* (ISO), selected from the ISO Data Archive, and having an IRAS 60/100μm color ratio of 0.2-1.4 and IRAS 60μm flux density between 0.1 Jy and 1300 Jy. This sample includes normal galaxies, starbursts, and active galactic nuclei (AGN) spanning a wide range of FIR colors and morphologies from early to late types. Seven fine structure emission lines are detected that arise in photodissociation regions (PDRs) ([OI] 63μm and 145μm, [CII] 158μm) or hot ionized HII regions ([OIII] 52μm and 88μm, [NIII] 57μm, [NII] 122μm, [CII] 158μm), including serendipitous detections of Milky Way [CII] 158μm. Molecular lines such as OH (53μm, 65μm, 79μm, 84μm, 119μm, 163μm) and H_2O (58μm, 66μm, 75μm, 101μm, 108μm) as well as an unidentified line at 74.24μm are also detected in some of these galaxies.

Continuum fluxes at 52μm, 57μm, 63μm, 88μm, 122μm, 145μm, 158μm and 170μm are derived for a subset of galaxies whose FIR emission is constrained to the 75" LWS beam. I compare these fluxes to model fluxes derived from an infrared SED model for the dust continuum of normal galaxies. The FIR continuum derived from the LWS spectra match the expected model fluxes to within 25%. On average, the LWS continuum fluxes at 60μm and 100μm are compared and found to be 1% lower and 2% higher than corresponding IRAS Point Source Catalog fluxes. The continuum at 170μm is compared to ISOPHOT pointed and Serendipity Survey fluxes and agrees to within the 30% errors of the ISOLWS and ISOPHOT instruments at that wavelength.

For galaxies with FIR emission smaller than the LWS beam, I examine the statistical properties of the FIR fine structure lines and line ratios in varying ISM environments as measured by the 60/100μm and FIR/B ratios. The ratio [CII](158μm)/FIR declines with increasing 60/100μm and FIR/B, whereas [OI](63μm)/[CII] increases with 60/100μm, indicating that [OI] 63μm becomes more dominant than [CII] in the cooling of the ISM of warmer, more active galaxies. Similarly, [NII](122μm)/FIR decreases with increasing 60/100μm and FIR/B ratio while the [NII]/[CII] ratio is flat, possibly indicating that a large fraction of [CII] arises from HII regions where [NII] is produced or that ratio of PDR to diffuse ionized gas does not vary systematically with 60/100μm or FIR/B. The [OIII](88μm)/FIR ratio increases as the 60/100μm ratio increases, suggesting that warmer galaxies, populated by more HII regions, produce more global [OIII] emission, but the [OIII] (88μm)/FIR ratio shows an anticorrelation with FIR/B, decreasing with increasing FIR/B. This increase in [OIII] emission with increasing 60/100μm ratio, coupled with the decrease in [CII] emission in warmer galaxies, leads to a steady increase in the [OIII] (88μm)/[CII] ratio as the 60/100μm ratio increases and suggests that the [CII] emission from HII regions correlates to lower density, N^+ regions rather than higher density O^{++} regions that produce [OIII](88μm).

This sample is the largest collection of FIR lines ever assembled and represents 465 independent ISOLWS observations (TDTs), 1975 FIR line fluxes and upper limits,

and 800 continuum fluxes. Here I present the FIR line and continuum fluxes that will serve as a catalog for future studies of the ISM in these galaxies.

Subject headings: galaxies: general -- galaxies: ISM -- ISM: atoms -- ISM: lines and bands -- infrared: ISM: continuum

1. INTRODUCTION

Far-infrared (FIR) wavelengths provide the opportunity to observe dust-enshrouded galaxies without large extinction effects and offer many diagnostics of the physical conditions in the interstellar medium (ISM) of these galaxies. The *Kuiper Airborne Observatory* (KAO) provided early data on the far infrared fine structure lines that arise in photodissociation (PDR) and HII regions in galaxies. The *Infrared Astronomy Satellite* (IRAS) revealed the first view of the whole sky at 12μm, 25μm, 60μm, and 100μm and opened the door to a to a new era of space based infrared astronomy. With the launch of the *Infrared Space Observatory* (ISO; Kessler et al. 1996) the FIR properties of galaxies were observed with greater sensitivity than ever before. The Long Wavelength Spectrometer (LWS; Clegg et al. 1996) on ISO allowed the large-scale study of FIR atomic and molecular lines that supply new insight into the understanding of the ISM of these sources.

The LWS was used to obtain spectra of the primary diagnostic lines of the ISM in the FIR. These lines include [CII] 158μm, [OI] 145μm, [NII] 122μm, [OIII] 88μm, [OI] 63μm, [NIII] 57μm and [OIII] 52μm. Among these atomic and ionic fine structure lines, [CII] 158μm and [OI] 63μm are the dominant cooling lines for neutral interstellar gas and along with [OI] 145μm, probe the conditions in PDRs. Recent observations of [CII] in NGC 6946 (Madden et al. 1993; Contursi et al. 2002) also suggest that a significant fraction of the [CII] emission might originate in diffuse ionized gas in some galaxies. The emission lines from the ionized species: [NII] 122μm, [OIII] 88μm, [NIII] 57μm and [OIII] 52μm, originate in HII regions. Combined with PDR models (Tielens & Hollenbach 1985; Wolfire, Tielens & Hollenbach 1990; Kaufman et al. 1999) and HII region models (Rubin 1985; Rubin et al. 1994), these fine structure transitions can be used to derive gas temperatures, densities, and the intensity of the radiation fields in galaxies.

The LWS also observed a suite of molecular lines in galaxies including hydroxyl (OH; 53μm, 65μm, 79μm, 84μm, 119μm, 163μm), water (H_2O; 59μm, 67μm, 75μm, 101μm, 108μm), and carbon monoxide (CO (J=16-15); 163μm). From the detections of multiple transitions of these molecules, the column densities and abundances for OH, H_2O, and CO can be determined. Bradford et al. (1999) and Skinner et al. (1997) determined the column density and abundance of OH in NGC 253 and Arp 220, respectively. Numerous H_2O lines are observed and reported in Arp 220 by Fischer et al. (1999) as part of a sequence of infrared bright galaxies.

In this paper, I report on LWS observations of the seven FIR fine structure atomic and ionic lines, the FIR molecular lines, serendipitous detections of Milky Way [CII] 158μm, and the FIR continuum of 227 galaxies. The FIR lines in this paper comprise the

largest sample ever assembled and reduced in a uniform manner. Using the line fluxes derived in this paper, I compare the relationship of the FIR fine structure line ratios and lines normalized to the FIR to two indicators of star formation activity, the 60/100μm ratio and FIR/B ratio, and relate these findings to previous LWS studies (Malhotra et al. 1997, 2001; Leech et al. 1999; Fischer et al. 1999; Luhman et al. 1998; Negishi et al. 2001). From the continuum fluxes determined here, I compare the LWS continuum fluxes to IRAS 60μm and 100μm, ISOPHOT 170μm, and an infrared galaxy SED model (Dale et al. 2001, 2002).

This paper will provide the data and framework for future studies of the ISM in these galaxies including the derivation of the gas temperatures, densities, abundances, and radiation fields for galaxies unresolved by the LWS and provide insight into the global physical conditions of the ISM. The line and continuum fluxes derived in this paper also supply the data for studies of the individual components (HII regions, spiral arms, disk regions) of large galaxies resolved by the LWS. Using the line fluxes derived in this paper, Contursi et al. (2002) examine the physical conditions of these different galaxy components in NGC 1313 and NGC 6946 using PDR models (Kaufman et al. 1999).

Section 2 describes the sample of galaxies, while § 3 describes the observations and data analysis. In § 4, the FIR continuum data are presented and assessed from comparisons to a galaxy infrared SED model and IRAS and ISOPHOT data. The FIR line data and properties are presented in § 5. In § 6, the statistical trends seen in the line data are described and these trends are related to those found from previous studies. A summary of the main results and conclusions is given in § 7. Appendix A provides a description of the extended source correction and how it may be applied to the line and continuum fluxes for source extended in the LWS aperture. Appendix B describes the comparison of continuum fluxes derived from LWS observations to IRAS fluxes at 60μm and 100μm. Appendix C describes the comparison of 170μm LWS continuum fluxes to ISOPHOT 170μm Serendipity Survey fluxes.

2. THE SAMPLE AND DATA

The ISOLWS sample of galaxies selected for this paper is presented in Table 1 and lists the galaxy positions, recession velocities, morphologies, optical sizes, and the flux densities of these galaxies in the four IRAS bands along with the IRAS 60/100μm ratios. The positions, optical sizes, and velocities are taken from the NASA Extragalactic Database (NED).

The sample includes both normal and Seyfert galaxies that were initially selected by identifying galaxies in the IRAS Catalog of Galaxies and Quasars (CGQ). The galaxies identified from the CGQ range in 60μm and 100μm flux density from 1 Jy to 1300 Jy. The ISO Data Archive (http://www.iso.vilspa.esa.es/ida/index.html) was queried using this list, from which 198 galaxies were observed in the LWS L01 or L02 observing mode. Later, galaxies with IRAS fluxes less than 1 Jy or those with no cataloged IRAS flux were added to the sample in an attempt to make as large a galaxy sample as possible. With these considerations, another 29 galaxies were identified within the ISO Archive. Photometric mode L02 observations in which the grating remained in a fixed position are excluded from this sample. The large, nearby galaxies M31, the Large

Magellanic Cloud and Small Magellanic Cloud are excluded from this sample because the size of these three galaxies is over 100 times larger than the LWS beam.

Among these 227 galaxies, there are two distinct subsets. The criterion for the two subsets is based upon the FIR size of the galaxy. The galaxies in the first subset, containing 181 galaxies, are unresolved in the FIR with respect to the 75" LWS beam. This unresolved subset of galaxies is an extension of the combined sets of smaller samples observed with the LWS (Malhotra et al. 2001; Pierini et al. 1998; Luhman et al. 1998; Negishi et al. 2001) with additional sources added from the ISO Data Archive. The second subset consists of 46 galaxies resolved by the 75" LWS beam in the FIR. The data from this resolved subset of galaxies can be used to complement past studies (Stacey et al. 1991; Madden et al. 1993, 1997) of large galaxies with data taken from the KAO and ISO. The resolved and unresolved subsets are indicated in Table 1.

The galaxies in this sample are distributed across the entire sky. Figure 1 displays the galaxy distribution in Galactic coordinates. The clump of galaxies at (l,b)~(280°,74°) is the Virgo Cluster. Approximately 40 galaxies lie within the Zone of Avoidance, where $|b| < 20°$. Although there may be some serendipitous Galactic line and continuum emission in all directions of the sky, this serendipitous contamination is more likely in the galaxies within the ZOA in either the galaxy spectra or the spectra of an off-source position taken during these observations. This contamination of the observed line measurements by Milky Way emission is a concern, and a discussion of these detected Galactic emission lines follows in Section 5.

Using the POSS plates and other observations found within NED, Harold Corwin reexamined the optical morphology (RC3; de Vaucouleurs et al. 1991) for each galaxy (personal comm.). In Figure 2, the distribution of the optical morphological types for the two subsets is shown. Both the resolved and unresolved subsets span the range of early to late type galaxies. The unresolved subset contains a relatively large number of S0 galaxies while the resolved subset contains no elliptical, S0/a, or peculiar galaxies.

Most of the galaxies in both the unresolved and resolved subsets are relatively nearby, and Figure 3 shows the redshift distribution for both subsets. All galaxies in the resolved subset have an absolute redshift less than 2000 km/s. With the exception of a large bin (22/181) of galaxies with redshifts greater than 10000 km/s, most galaxies in the unresolved subset have redshifts less than 6000 km/s.

These galaxies also span a wide range of physical properties such as dust temperature and star formation activity, measured from the IRAS colors. Figure 4 shows the distribution of measured flux densities at 60μm and 100μm for the resolved and unresolved galaxies in this paper with IRAS detections taken from Table 1. The distribution of the two subsets is different. At 60μm, both the resolved and unresolved galaxy distributions peak around 10 Jy, but the resolved galaxies span a different flux density range (~1-1300 Jy) than the unresolved galaxies (~0.2-150 Jy). At 100μm, the distribution of the unresolved and resolved galaxy subsets peak around between 10 and 50 Jy. The distribution of 100μm fluxes in the resolved and unresolved galaxies is similar, with the unresolved galaxies spanning a more continuous range of fluxes between 1-1000 Jy. The distribution of the 60/100μm ratio and FIR are displayed in Figure 5. The 60/100μm ratio is an indicator of the typical heating intensity of dust in galaxies and may also suggest the star formation activity of a galaxy. Lower 60/100μm ratios typically correspond to quiescent galaxies, whereas, higher 60/100μm ratios

indicate either a higher rate of star formation or perhaps the presence of an AGN. FIR is defined as FIR = 1.26×10^{-14} [2.58 $F_\nu(60\mu m)$ + $F_\nu(100\mu m)$] W m^{-2}, where $F_\nu(60\mu m)$ and $F_\nu(100\mu m)$ are the 60μm and 100μm IRAS flux densities in Jy (Helou et al. 1988). The unresolved and resolved galaxy subsets peak near 60/100μm ratios of 0.5 and 0.4, respectively, and the resolved subset does not contain many warm galaxies with 60/100μm ratios greater than 0.7. The distribution of FIR values for the two subsets spans five orders of magnitude with a peak between 10^{-12} and 10^{-13} W m^{-2}. The resolved galaxies reach FIR values as high as 10^{-10} and 10^{-11} W m^{-2}, an order of magnitude larger than the unresolved galaxies. In Figure 6, the IRAS 12/25μm ratio is plotted against the 60/100μm ratio for the resolved and unresolved subsets. The sequence of infrared colors in Figure 6 was associated with a sequence of star formation activity in galaxies (Helou 1986) and dust-heating intensity (Boulanger et al. 1988) with the upper left populated by quiescent galaxies and the lower right by warmer, more active galaxies.

3. OBSERVATIONS AND DATA ANALYSIS

Observations were made using the LWS in medium-resolution grating mode (L01, L02, 43-197μm, $\lambda/\Delta\lambda$~200). The LWS consists of ten detectors with spectral overlap for adjacent detectors. In the grating mode of the LWS, the spectral resolution is about 0.29μm for the 10μm-wide short-wavelength detectors (SW1-SW5) and 0.60μm in the 20μm-wide long-wavelength detectors (LW1-LW5). The L01 Astronomical Observation Template (AOT) is a full scan of the grating that results in a spectrum over the entire range of the LWS. The L02 AOT produces spectra for up to ten wavelengths, specified by the observer. In this mode, data are recorded for all ten detectors while the specified wavelengths are being scanned, producing sparsely sampled spectra over the range of the LWS.

All guaranteed and open time observations for 227 galaxies were extracted from the ISO Data Archive and processed through the LWS Pipeline Version (OLP) 7.0 or 8.7. Between Pipeline Version 7.0 and the final LWS Pipeline, Version 10.0, slight improvements in the photometric model are made, but these changes have minor effects on the calibration of the L01 and L02 grating mode AOTs. These changes yield improvements in the flux accuracies by a few percent but do not significantly alter the resulting line and continuum fluxes that are derived from Pipeline 7.0.

The continuum fluxes in the LWS spectra are significantly affected by the errors in the dark current that can be of the same order as the continuum. Many of the galaxies in this sample are in this faint flux regime ($F_\nu(60\mu m)$ < 50 Jy in the 75" LWS beam). As the dark currents are only additive in nature, they do not affect the line flux estimates. To correct for this, the dark currents were re-estimated and removed one at a time by hand through visual inspection using the LWS Interactive Analysis (LIA; Hutchinson et al. 2001). The data were then corrected detector by detector for any evident instrumental responsivity variations and flux calibrated to the LWS calibration source Uranus, applied using LIA. Glitches due to cosmic rays were removed by hand from the data using the ISO Spectral Analysis Package (ISAP; Sturm et al. 1998) by plotting spectral scans and identifying bad data points through the characteristic appearance of falling glitch trails. Depending on the quality of the observation of a galaxy, between 15% and 20% of the data were typically discarded. Spectral scans were co-added and averaged together using

a 3σ clip in spectral bins of about 0.05μm. For full-grating L01 observations, a sinusoidal fringe associated with internal reflection and interference within the LWS instrument may arise (Gry et al. 2001, Swinyard et al. 1998). The fringes are usually less than 5% of the continuum and do not severely affect the line and continuum measurements. These fringes were removed using a defringing algorithm supplied within ISAP. The LWS data also suffer from transients. When the grating is scanned between the forward and reverse directions, a small (<5%) detector memory effect (Gry et al. 2001) may be visible between the two scan directions. This memory effect is due to different response times for the detectors depending on whether the signal increases or decreases with time and is most visible in the SW1, SW2, and LW2 detectors during L01 observations. Currently, there is no correction for these memory effects. When these memory effects are present in the data, each scan direction was averaged separately, and the line and continuum fluxes for each scan direction were measured before estimating the final fluxes and errors in the manner described in Sections 4 and 5. An additional source of error occurs for extended sources where the variation in the LWS beam from detector to detector might cause a mismatch between adjacent detectors by up to 30% depending on the extent and structure of the galaxy. With the application of an extended source correction, this mismatch might eventually be corrected. The data presented in this paper are based on the point source calibration of the pipeline and no correction for extended sources has been applied due to the uncertainty in this correction. See Appendix A for the definition and discussion of the extended source correction.

Through the use of LIA and ISAP, the improvement in the overall quality of the data from the original pipeline Auto-Analysis Result (AAR) product is substantial. By re-estimating the dark currents, the appearance of negative fluxes in most of these observations was removed. Through the re-estimation of the dark currents and gain corrections and careful glitch removal, the match between overlapping detectors was improved, thus producing more continuous spectra, shown in Figure 7. Any remaining spectral mismatch between adjacent detectors may be the result of residual errors in the dark current subtraction or beam uncertainties from detector to detector. Using LIA and ISAP, the line and continuum calibration is improved by about 10% to 15%.

4. THE CONTINUUM DATA

The "monochromatic" continuum fluxes were derived from the LWS spectra by fitting a 2-5μm linear baseline through the spectra surrounding the wavelengths 52μm, 57μm, 63μm, 88μm, 122μm, 145μm, 158μm, and 170μm. Continuum fluxes were measured only for the well-calibrated LWS spectra when spectra were available at these wavelengths. Continuum fluxes could not be derived in some L02 observations that had no spectra at these wavelengths. If the observations were affected by changes in the responsivity and dark current caused by warm-ups in the long wavelength detectors, no continuum flux was derived. These continuum fluxes and associated errors are listed in Table 2. Because of the uncertainty of off-axis continuum contributions in extended sources, only fluxes for galaxies unresolved by the LWS beam are listed (see Appendix A for an explanation of extended sources).

Since the L02 observations do not have much overlap between detectors, it is difficult to properly estimate the continuum. In order to test the consistency of the

continuum of the L02 observations, the continuum were compared from observations of the 158μm and 63μm line for galaxies that had a pointing at the same position in both the L01 and L02 AOTs. The continuum flux was taken from the linear baseline that was used for the fit to the lines at 158μm and 63μm for these observations. The continuum in the L02 observations accurately reproduces the continuum measured in the L02 AOT to 5% for continuum fluxes down to 10 Jy. The continuum correlation between the two AOTs holds for fluxes below 10 Jy, but the dispersion is this relation increases by a factor of two. Therefore, the reliability of the L02 continuum appears to be consistent with the L01 continuum although some uncertainties exist from the dark or gain calibration that cannot be easily characterized due to the lack of overlapping spectra from adjacent detectors. These uncertainties are evident from the increased dispersion in the low-flux limit below 10 Jy.

The continuum errors quoted in Table 2 are a combination of the measurement and calibration uncertainties (typically 15-20%). In most observations, the calibration uncertainties are the dominant source of uncertainty in the continuum fluxes, but in the low flux limit (<10 Jy), the measurement uncertainties become dominated by uncertainties in the dark current. The detector dark currents are of the same order as the continuum in this flux regime. The result of these errors in the dark current is seen below 10 Jy in the comparisons of LWS data to IRAS at 60μm and 100μm described in Appendix B and to ISOPHOT-derived fluxes at 170μm in Appendix C. Although the comparisons to IRAS and ISOPHOT show an excellent overall agreement to the LWS continuum fluxes within the LWS 20% uncertainties down to fluxes below 10 Jy, the dispersion in these relationships increases by as much as a factor of two below 10 Jy. The increase in the dispersion below 10 Jy is due to the large dark current uncertainties. Therefore, although there may be large uncertainties, the measured continuum fluxes below 10 Jy are included in Table 2 because there are no biases in the agreement of the LWS fluxes with IRAS and ISOPHOT in this low-flux limit.

4.1 Comparison with Galaxy Infrared SED Model

The data for the subset of galaxies smaller than the LWS aperture discussed in the previous section were compared to a semi-empirical model for the infrared spectral energy distribution of normal star-forming galaxies between 3 and 1100μm (Dale et al. 2001, 2002). The comparison of the LWS and SED model fluxes provides a consistency check of the LWS continuum fluxes, especially at the longer wavelengths where few continuum measurements from other observatories exist. The SED model is based on the combination of emission curves for large and very small grains and aromatic feature carriers for varying interstellar radiation fields. The model is constrained by IRAS and ISOCAM broadband photometric and ISOPHOT spectrophotometric observations of a sample of 60 normal, star-forming galaxies (Helou et al. 1996; Dale et al. 2000, Malhotra et al 2001). In this model, a sequence of global star formation activity level is formed as galaxies are sorted according to their 60/100μm ratio. The synthetic SEDs cover a range of dust environments in different radiation fields. The SEDs are combined assuming a power-law distribution in a given galaxy of dust mass over heating intensity. The LWS continuum agrees with the predicted model fluxes for these galaxies to within 25% at 52μm, 57μm, 63μm, 88μm, 122μm, 145μm, 158μm, and 170μm and is presented in

Figure 8. The SED model and the comparison with the LWS continuum are explored further in Dale et al. (2002).

5. THE LINE DATA

All spectral lines in this paper are unresolved ($\Delta v \sim 1500$ km/s), thus, the line fluxes were calculated assuming the line profile to be dominated by a Gaussian instrumental profile (FWHM=0.29μm for $\lambda < 93\mu m$, 0.60 for $\lambda > 80\mu m$). For wavelengths between 80 and 93μm, the spectral resolution is dependent on which of the two overlapping detectors (SW5, LW1) the line was measured. A Gaussian has been shown to fit the LWS instrumental profiles within 2% (Gry et al. 2001). Example lines from this sample with various signal-to-noise ratios are displayed with a Gaussian fit in Figure 9. A detected line in this sample is defined as one that has a flux at the 3σ or higher confidence level. The statistical error associated with each line was calculated by multiplying this effective instrumental width and the r.m.s. of a linear baseline fit to the data. The dominant error for most observations is the systematic flux error that is taken from the pipeline processing. This error is a combination of the dark current, illuminator, and Uranus model calibration errors. The total error is calculated by adding the statistical and systematic errors in quadrature. The total error is typically between 10% and 20%, depending on the quality of the observation. In the case of non-detections, 3σ upper limits were calculated by multiplying the effective instrumental width and the r.m.s. of the baseline fit to the data. The galaxies from previous studies (Malhotra et al. 1997, 2001; Leech et al. 1999; Negishi et al. 2001) are included as a subset of the larger sample presented here, but are independently reduced in the manner described in §3. In general, the line fluxes presented in this paper for those galaxies agree to within 30% with the line fluxes derived in those studies. The lines, rest wavelengths, and transitions for this sample are listed in Table 3.

5.1 Far Infrared Fine Structure Lines

The far infrared fine structure lines [CII] 158μm, [OI] 145μm, and [OI] 63μm presented in Table 3 have been used to model the density and radiation intensity in photo-dissociation regions (PDR) in previous studies (Tielens & Hollenbach 1985; Wolfire et al. 1990; Hollenbach et al. 1991; Hollenbach & Tielens 1997; Kaufman et al. 1999). The [CII] 158μm, [OI] 63μm, and [OI] 145μm lines act as the primary coolants to the dense ($n \sim 10\text{-}10^5$ cm^{-3} or more), warm ($T \sim 100\text{-}1000$ K), neutral media. The remaining far infrared fine structure lines listed in Table 3 ([NII] 122μm, [OIII] 52μm and 88μm, and [NIII] 57μm) are important in the understanding of HII regions. From these HII region lines, the electron densities n_e and the effective temperature of the ionizing stars can be determined using HII region models (Rubin 1985; Rubin et al. 1994). The fluxes and associated errors for these seven far infrared fine structure line measurements are given in Table 4 with the resolved and unresolved subsets noted in the table. For the purposes of this paper, I examine the statistical trends in the data for the subset of galaxies unresolved by the LWS beam in §6 and compare these results to those of earlier studies (Malhotra et al. 2001; Luhman et al. 1998; Leech et al. 1999; Negishi et al. 2001).

5.1.1 [CII] 158μm

The [CII] fine structure transition at 157.71μm is the dominant coolant of the neutral interstellar medium because of its low ionization potential (11.26eV) and traces photodissociation regions (PDRs). Because of its low ionization potential, [CII] will lie in neutral surface layers of far-UV illuminated neutral gas clouds. [CII] 158μm is also easy to excite ($\Delta E/k \sim 91$ K) and therefore cools the warm, neutral gas (Tielens & Hollenbach 1985; Wolfire et al. 1990). In addition to PDRs, significant contributions to [CII] emission can arise from ionized gas in diffuse HI and dense HII regions, although it is unclear how much [CII] comes from these regions. (Madden et al. 1993, 1997; Petuchowski & Bennett 1993; Heiles 1994; Sauty, Gerin & Casoli 1998). [CII] is detected in 153 galaxies and 3σ upper limits are determined in another 17 galaxies in the unresolved subset of galaxies. [CII] is detected in all 46 galaxies of the resolved subset of galaxies.

5.1.2 [OI] 145μm & 63μm

Oxygen has two fine structure transitions at 63μm and 145μm and has an ionization potential of 13.62 eV. Atomic oxygen is only found in neutral regions and exists deeper into clouds than [CII]. [OI] becomes the main coolant in warmer and denser environments ($T > 200$ K and $n > 10^5$ cm^{-3}) due to its higher excitation energies and critical densities ($\Delta E/k \sim 228$ K; $n_{crit} \sim 8.5 \times 10^5 (T/100)^{-0.69}$ [H] (cm^{-3}) for [OI] 63μm and $\Delta E/k \sim 325$ K; $n_{crit} \sim 1 \times 10^5 (T/100)^{-0.57}$ [H] (cm^{-3}) for [OI] 145μm). In this sample, the [OI] transitions are always observed in emission with the exception of Arp 220. The case of Arp 220 is discussed as part of a progression of emission and absorption line characteristics in a spectroscopic survey of infrared bright galaxies (Fischer et al. 1999). The [OI] 63μm line is detected in 93 galaxies with 3σ upper limits for an additional 25 in the unresolved subset and detected in 28 galaxies with another three galaxies with 3σ upper limits in the resolved subset of galaxies. The much fainter [OI] 145μm line is detected in 20 galaxies with 3σ upper limits in another 15 in the unresolved subset and is detected in 9 galaxies with another two 3σ upper limits in the resolved subset.

5.1.3 [NII] 122μm

Nitrogen has an ionization potential of 14.5 eV, and the [NII] 122μm line has a critical electron density of 3.1×10^2 cm^{-3}. Since its ionization potential is greater than that of hydrogen, the [NII] 122μm transition arises only in ionized HII regions. The *Cosmic Background Explorer* (COBE; Boggess et al. 1992) and the KAO provided the first astronomical detections of the [NII] 122μm line (Wright et al. 1991; Colgan et al. 1993). This sample greatly expands the number of extragalactic [NII] detections from earlier studies (Malhotra et al. 2001). The [NII] 122μm line is detected in 38 galaxies and 3σ upper limits in 41 of the galaxies in the unresolved subset. For the resolved subset of galaxies, [NII] is detected in 16 galaxies and 3σ upper limits in another 2.

5.1.4 [OIII] 88μm & 52μm

OII has an ionization potential of 35 eV. Due to the high ionization potential, the two transitions of [OIII] at 88μm and 52μm occur in the HII regions in galaxies. Using the methodology of Rubin et al. (1994), the ratio of these two lines

[OIII] 88μm/[OIII] 52μm, can be used to derive the average electron density n_e of these regions within galaxies (Duffy et al. 1987; Carral et al. 1994; Lord et al. 1996; Malhotra et al. 2001; Hunter et al 2001). The [OIII] 88μm line is detected in 52 galaxies and 3σ upper limits in 14 galaxies for the unresolved subset. The [OIII] 88μm line is detected in 16 galaxies and 3σ upper limits for 1 galaxy in the resolved subset. The lower S/N [OIII] 52μm line is detected in 11 galaxies with 3σ upper limits for another 22 in the unresolved subset and detected in 5 galaxies and 3σ upper limits in an additional 6 galaxies for the resolved subset.

5.1.5 [NIII] 57μm

NII has a high ionization potential of 47.45 eV and therefore, the [NIII] 57μm transition is only found in the ionized HII regions of the galaxies in this sample. The ratio [NIII] 57μm/[NII] 122μm provides a measure of the effective temperature T_{eff} (Rubin et al. 1994). The LWS allowed a more detailed study of the faint [NIII] 57μm line since there are few detections of this line in the literature (Duffy et al. 1987; Malhotra et al. 2001). For the unresolved subset of galaxies, the [NIII] line is detected in 9 galaxies and 3σ upper limits in another 24 galaxies. The [NIII] line is detected in 2 galaxies and 3σ upper limits are determined for 6 galaxies in the resolved subset.

5.2 Molecular Lines

Molecular lines are present in a few of the galaxies observed in this sample. In general, the line transitions of hydroxyl (OH; 53μm, 65μm, 79μm, 84μm, 119μm, 163μm), water (H_2O; 59μm, 67μm, 75μm, 101μm, 108μm), and carbon monoxide (CO; 163μm) listed in Table 3 are found in the most infrared luminous galaxies in Table 1 with IRAS 60μm fluxes typically higher than 100 Jy. These molecular lines are observed in both emission and absorption for these galaxies. Table 5 lists the fluxes derived for these lines.

5.2.1 H_2O

Water (H_2O) has been detected in two galaxies in this sample. The unresolved 101μm ortho-para-H_2O pair is found in absorption for NGC 4945. All five H_2O transitions reported in this paper are observed in absorption in Arp 220.

5.2.2 OH

Six transitions of Hydroxyl (OH) have been detected in this sample. The OH 53μm transition is measured in absorption and the 163μm transition in emission for NGC 253 and Arp 220. All galaxies in Table 5 show OH from the ground level at 119μm, and with the exception of the archetypical Seyfert 2 galaxy NGC 1068, this transition is measured in absorption. In fact, all the OH lines detected (79μm, 119μm) for NGC 1068 are observed in emission, suggesting a unique excitation environment (Spinoglio et al. 1999). The ultraluminous Seyfert 1 galaxy Mrk 231 shows an absorption line cascade at 84μm and 119μm. The 53μm, 119μm, and 163μm OH transitions in NGC 253 (Bradford et al. 1999) and the 84μm and 119μm transitions in Mrk 231 (Harvey et al. 1999) have been previously reported. In Arp 220, all six transitions of OH reported in this paper are

detected. An absorption line cascade is suggested with the presence of the 65μm, 84μm, and 119μm transitions. Cross ladder transitions at 53μm and 79μm are also observed.

5.3 Unidentified Line

An unidentified emission line at 74.24μm also reported in NGC 7027 (Liu et al. 1996) and RWC 103 (Oliva et al. 1999) is detected in NGC 1068. The line flux and associated error for this line is listed in Table 5.

5.4 Serendipitous Galactic [CII] 158μm

The Far-Infrared Absolute Spectrophotometer (FIRAS) on the COBE satellite conducted an unbiased survey of the far-infrared emission from our Galaxy. The FIRAS spectral-line survey included the emission lines from [CII] 158μm, [NII] 122μm and 205μm, [CI] 370μm and 609μm, and CO J=2-1 through J=5-4 with a resolution of 7° and were first reported by Wright et al. (1991). The [CII] 158μm line had sufficient strength to be mapped by FIRAS, and Bennett et al. (1994) presented more detailed maps of this emission line. The all-sky maps of the [CII] 158μm line given in these papers show the highest concentration at low galactic latitudes ($|b| < 20°$). Of the approximately 40 galaxies in this sample in this region, eight have spectra with detectable [CII] associated with our Galaxy. An additonal four observations with $|b| > 20°$ show Galactic [CII]. These high latitude detections may either be due to diffuse Galactic emission (Bock et al. 1993), the Warm, Ionized Medium (WIM; Petuchowski & Bennett 1993), or high latitude molecular clouds (Magnani et al. 1996). These observations of Milky Way [CII] are listed in Table 6.

The IRAS Sky Survey Atlas (ISSA) images at 60μm and 100μm reveal extended Galactic emission in the same direction as the four high latitude [CII] detections. The ISSA maps at 100μm and the LWS line spectra containing both Galactic [CII] and [CII] associated with three galaxies (ESO 173-G015, NGC 1614, UGCA 332) is presented in Figure 10. The [CII] line associated with the background galaxy is located at the redshift of the galaxy, whereas the foreground Galactic [CII] is at the rest wavelength of 157.71μm. Reach et al. (1998) describe the location of the UGCA 332 observation as a high latitude warm infrared excess HII region around the nearby B star Spica using far-infrared (60-240μm) data from the COBE Diffuse Infrared Background Experiment (DIRBE) and the Leiden-Dwingeloo H I survey (Hartmann & Burton 1997), confirming the foreground source of this line emission and seen in Figure 10.

For the [CII] line observations listed in Table 4, some contamination from line blending may occur between [CII] of the observed galaxy and [CII] associated with the Milky Way if the galaxy's radial velocity is smaller than the velocity resolution of the LWS ($|v| < 1500$ km/s). Therefore, the amount of Galactic [CII] contamination must be determined for the LWS observations. The expected intensity of the Galactic [CII] emission in the LWS aperture for these observations is estimated by two methods and then compared to the LWS measurements. The first method uses the COBE prediction from Bennett et al. (1994)

$$I(C^+ 158\mu m) = (1.43 \pm 0.12) \times 10^{-6} \csc |b| \text{ ergs cm}^{-2} \text{ s}^{-1} \text{ sr}^{-1} \quad (1)$$

The second method assumes [CII] to be approximately 0.5% of the background Galactic FIR (Shibai et al. 1991; Nakagawa et al. 1995) in the region surrounding these observations. The background Galactic FIR is measured using the mean IRAS 60μm and 100μm flux densities from a 30' × 30' field. The estimated [CII] intensity from the COBE and IRAS observations agree to within a factor of 2-6 with the LWS observations for all galaxies in Table 6 except Maffei 2 which lies close to the Galactic plane.

The COBE all-sky maps of [CII] show strong concentrations of Milky Way [CII] at low galactic latitudes ($|b| < 20°$), thus, Galactic [CII] contamination of the observations in Table 4 is possible for nearby ($|v| < 1500$ km/s), low galactic latitude ($|b| < 20°$) galaxies. Nineteen galaxies in this sample meet these two criteria. Eight of nineteen have an off position associated with each observation, where each off position is typically 4'-6' away from the observed galaxy. Five of these eight observations have detectable Milky Way [CII] and are listed in Table 6.

The intensity of the Galactic [CII] line is compared to the total [CII] in an LWS aperture for six galaxies (five low latitude) with $|v| < 1500$ km/s where [CII] is found in a reference position away from the galaxy. The [CII] associated with the Milky Way is between 10% and 25% of the total [CII] in the LWS aperture for these six galaxies, and the [CII] line fluxes listed in Table 4 for these six galaxies have had the background Milky Way [CII] from Table 6 removed. For the remaining eleven galaxies with $|v| <$ 1500 km/s and $|b| < 20°$, the contamination from Milky Way [CII] is expected to be no more than 25%, estimated from Table 6. For the 55 higher latitude ($|b| > 20°$) galaxies with $|v| < 1500$ km/s and no off-source observation, any Milky Way [CII] contamination is likely much less than 10%.

6. STATISTICAL TRENDS IN THE LINE DATA

In this section, the statistical trends in the FIR fine structure line fluxes from Table 4 are examined for the 181 galaxies in the unresolved subset of this sample. The observed lines normalized to the far-infrared continuum (FIR) and line ratios are examined across a broad range of 60/100μm and FIR/Blue ratios. The 60/100μm ratio is an indicator of the dust heating intensity in galaxies, possibly suggesting the star formation activity in a galaxy. The FIR/B ratio compares the luminosity reprocessed by dust to that of escaping starlight, indicating star formation activity and optical depth along with the effects of extinction.

The data for the figures in this section were divided into five bins for the 60/100μm ratio and four bins for the FIR/B ratio. These bins are 0-0.3, 0.3-0.6, 0.6-0.9, 0.9-1.2, and 1.2-1.6 for 60/100μm and –3 to -1, -1-0, 0-1, and 1-3 for FIR/B. A median is calculated for each bin using only the 3σ line detections in each bin. If a bin contained an even number of points, an average between the two middle points of the median in the bin is calculated.

6.1 [CII]/FIR

Previous studies (Malhotra et al. 1997, 2001; Leech et al. 1999; Negishi et al. 2001) of the [CII](158μm)/FIR ratio for galaxies reveal a trend with dust heating intensity as measured by 60/100μm and FIR/B ratios. Figure 11 shows the [CII]/FIR for the 181 galaxies of the unresolved subset of the sample presented in this paper, plotted

according to morphological type and exhibit the same trends for all types. A [CII]/FIR of 0.1%-1% characterizes normal and starburst galaxies between 60/100μm ratios of 0.3 and 0.8 and decreases with increasing 60/100μm, confirming earlier studies with fewer galaxies (Crawford et al. 1985; Stacey et al. 1991; Malhotra et al. 1997, 2001). Leech et al. (1999) report a lower [CII]/FIR of 0.1%-0.5% than that found in normal and starburst galaxies for a sample of relatively quiescent galaxies in the Virgo Cluster (60/100μm ≤ 0.4). As the dust temperature increases for the most active galaxies (60/100μm ≥ 0.8), the [CII]/FIR continues to decrease from 0.1% to 0.01% in Figure 11. The elliptical galaxies NGC 6958, NGC 1052, and NGC 5866 are a factor of 2-5 lower than typical values of [CII]/FIR for normal galaxies as first reported by Malhotra et al. (2000). However, the remaining early-type galaxies (ellipticals and lenticulars) appear to have similar [CII]/FIR ratios to normal galaxies in Figure 11. [CII] emission in irregular galaxies is higher relative to the [CII] emission in spiral galaxies of the same FIR color temperature shown in Figure 11, also noted by Hunter et al. (2001).

There is a large spread in the [CII]/FIR ratio for a given 60/100μm and FIR/B ratio. Despite this, there are several observed trends in the [CII]/FIR shown in Figure 11 and several possible explanations for these trends in galaxies.

1. The [CII]/FIR peaks for normal, star-forming galaxies with a 60/100μm ratio of 0.3-0.6 and FIR/B ratio between 0.1 and 1, consistent with earlier studies (Malhotra et al. 1997, 2001; Negishi et al. 2001). These galaxies have a higher fraction of intermediate-mass stars that are efficient at producing UV and [CII] line emission, thus, causing the peak for these galaxies.

2. The [CII]/FIR ratios for quiescent galaxies below a 60/100μm ratio of 0.3 and FIR/B ratio of 0.1 are, on average, similar to or slightly less than those for normal, star-forming galaxies. There is some evidence for lower [CII]/FIR ratios in the quiescent galaxies of the Virgo Cluster as suggested in this study and Leech et al. (1999). Quiescent galaxies with this range of 60/100μm and FIR/B have a larger old low-mass stellar population than normal galaxies, and produce less UV and [CII] line emission, causing a possible decrease in the observed [CII]/FIR ratio.

3. The [CII]/FIR decreases with increasing 60/100μm and FIR/B ratio. This trend has been seen within our Galaxy (Nakagawa et al. 1995; Bennett et al. 1994) and is not surprising for a sample of galaxies spanning a large range of 60/100μm and FIR/B ratios. Galaxies with 60/100μm ratios greater than 0.6 and FIR/B ratios greater than 1 have increasingly warmer dust temperatures, most likely due to more extreme star formation. These active galaxies have a large proportion of massive O stars that produce hard UV radiation. Several explanations from previous studies have been offered for the decrease in the [CII]/FIR ratio in active galaxies with the warmest dust temperatures. Malhotra et al. (2001) propose that the decrease in [CII]/FIR is due to the dust grains becoming more positively charged and less efficient at heating the gas for high ratios of UV flux to gas density (G_0/n) according to detailed PDR models (Tielens & Hollenbach 1985). Negishi et al. (2001) attribute this decrease in [CII]/FIR to either an increase in the collisional de-excitation of the [CII] transition at high densities or a decrease

in the ionized component of the [CII] emission. For a small sample of ultraluminous infrared galaxies (ULIGs) Luhman et al. (1999) report a deficiency of [CII], consistent with the decrease in the [CII]/FIR ratio at high 60/100μm ratios and explain this deficiency as the result of a soft UV radiation field from a stellar population dominated by old, low mass stars due to an aging starburst because fewer photoelectrons are being generated.

6.2 [OI](63μm)/FIR

The [OI](63μm)/FIR ratio for galaxies shows no trend with 60/100μm and a slight decreasing trend with FIR/B as displayed in Figure 12 for the 181 galaxies of the unresolved subset, plotted according to morphological type. An [OI](63μm)/FIR of 0.05%-1% characterizes these galaxies. Although [CII] tends to decrease with increasing 60/100μm, the same is not found for [OI](63μm)/FIR, consistent with earlier studies by Malhotra et al. (2001) and Negishi et al. (2001). Therefore, as the heating environment in galaxies gets warmer, [CII] becomes less dominant while [OI] (63μm) becomes more important in the cooling of the ISM.

6.3 [NII]/FIR

The [NII](122μm)/FIR ratio for galaxies reveals a trend with dust temperature as measured by the 60/100μm ratio (Malhotra et al. 2001). The [NII]/FIR for the 181 galaxies of the unresolved subset in this sample, plotted according to morphological type, is presented in Figure 13. A [NII]/FIR of 0.01%-0.1% characterizes these galaxies. The [NII] follows a similar decreasing trend to [CII] with 60/100μm and FIR/B as suggested in Figure 13. There is a clear decrease in [NII]/FIR as 60/100μm and FIR/B increase for spirals and irregulars. For morphologies other than spirals and irregulars, there are few detections of [NII] and no trend exists. From COBE observations of the Milky Way, a proportionality between [CII] and [NII] 205μm was found (Bennett et al. 1994), therefore, it is not surprising that [NII] 122μm and [CII] in galaxies exhibit some of the same characteristics over a broad range of heating environments. This decrease in [NII]/FIR with increasing 60/100μm and FIR/B possibly suggests that a large fraction of [CII] arises from HII regions where [NII] originates or that the ratio of PDR to diffuse ionized gas does not vary systematically with 60/100μm or FIR/B.

6.4 [OIII] 88μm/FIR

The [OIII](88μm)/FIR ratio for the galaxies in the unresolved subset is presented in Figure 14. An [OIII]/FIR of 0.03%-2% characterizes this sample. Although there is a large scatter among the data, there seems to be an increase in [OIII]/FIR as the 60/100μm ratio increases in Figure 14a. On average, there is relatively more [OIII] emission in warmer galaxies due to a larger number of HII regions in these galaxies. This overall increase in the [OIII]/FIR ratio is also noted in Negishi et al. (2001) for a smaller set of galaxy observations. In Figure 14b, the [OIII]/FIR appears to decrease as the FIR/B ratio increases. Malhotra et al. (2001) pointed out this anticorrelation between [OIII]/FIR and FIR/B, but it was attributed to the observations of two irregular galaxies in their sample. In this study, many new observations of the [OIII] (88μm) line are included, and a decreasing trend in [OIII]/FIR with increasing FIR/B is discovered.

6.5 [OI] 63μm/[CII]

In Figures 11 and 12, [CII] emission was shown to decrease with increasing 60/100μm and FIR/B while [OI] 63μm emission remained steady with 60/100μm and FIR/B. In Figure 15, the [OI] 63μm/[CII] ratio is plotted against 60/100μm and FIR/B, and a rise in [OI]/[CII] ratio is found as 60/100μm increases for all morphologies but no conclusive trend in the [OI]/[CII] ratio is found as FIR/B increases. From Figure 15a, [OI] 63μm begins to dominate cooling in the ISM of warmer galaxies (60/100μm ≥ 0.8), consistent with the results reported by Malhotra et al. (2001).

6.6 [NII]/[CII]

The [NII]/[CII] ratio remains relatively constant across a broad range of 60/100μm and FIR/B for all morphological types as shown in Figure 16 for the 181 galaxies in the unresolved subset of galaxies presented in this paper. The median value of the [NII]/[CII] for this sample is 0.11 when both lines have been detected, consistent with what COBE observed for the Milky Way (Wright et al. 1991; Bennett et al. 1994), but lower than what models predict if [CII] were only produced in HII regions (Rubin 1985). The similar decreasing behaviors in the [CII]/FIR and [NII]/FIR ratios with increasing 60/100μm and FIR/B ratios shown in Figures 11 and 13 along with Figure 16 point to the suggestion that a large fraction of [CII] arises from HII regions where [NII] originates, thus, causing the [NII]/[CII] ratio, on average, to be nearly constant across a broad range of heating environments.

6.7 [OI] 145μm/[OI] 63μm

The [OI] 63μm is generally optically thick, whereas the [OI] 145μm line is optically thin. The [OI] 145μm/[OI] 63μm measures the gas temperature and the optical depth in the 63μm line and rises as the gas temperature increases (Tielens & Hollenbach 1985; Kaufman et al 1999). There are few [OI] 145μm line observations presented in this paper, most of low S/N. The low S/N [OI] 145μm line has few detections in this sample, therefore, the [OI] 145μm/[OI] 63μm ratio has no clear trend with the 60/100μm or FIR/B ratios as displayed in Figure 17 for the unresolved subset of galaxies with either a 3σ detection or upper limit for the [OI] 145μm line and a detection for the [OI] 63μm line. Hunter et al. (2001) noted an increase in the [OI] 145μm/[OI] 63μm with increasing FIR/B ratios between –0.3 and 1 and attributed this increase to an indication of the optical depth effects for {OI] 63μm. The same increase is found in this study for FIR/B ratios between -1 and 1 before [OI] 145μm/[OI] 63μm decreases for FIR/B ratios larger than 1.

6.8 ([OI] 63μm + [CII]) / FIR

The gas heating efficiency of galaxies is measured by ([OI] 63μm + [CII])/FIR (**REFERENCE**?) and is plotted against the 60/100μm ratio and FIR/B for the unresolved subset of galaxies in the sample discussed in this paper in Figure 18. The ([OI] 63μm + [CII])/FIR ratio shows no trend with 60/100μm and a decreasing trend with FIR/B. For a sample of normal galaxies dominated by spirals, Malhotra et al. (2001) noted a decrease in this ratio as 60/100μm increased. Although the entire sample of galaxies does not appear to decrease in ([OI] 63mm + [CII])/FIR as the 60/100mm ratio increases, the

spiral galaxies show evidence for a decline in this ratio in warmer dust environments. The decrease in the ([OI] 63μm + [CII])/FIR with increasing FIR/B is a result of the decrease in [CII] emission shown in Figure 11.

6.9 [OIII] 88μm/[CII]

In Figures 11a and 14a, a decrease in [CII] and an increase in [OIII] emission were shown with increasing 60/100μm ratio. Accordingly, the [OIII]/[CII] ratio increases with increasing 60/100μm ratio, as presented in Figure 19a. This is an interesting correlation since [OIII] originates in HII regions as does [NII] (122μm). While the [NII]/[CII] ratio did not show a correlation with the 60/100μm ratio in Figure 16a, the [OIII]/[CII] ratio does. This suggests that the contribution to the [CII] emission from HII regions originates in lower density, N^+ and O^+ regions rather than the higher density O^{++} regions that produce [OIII] (88μm). In comparison, [CII] and [OIII] were shown to decrease with increasing FIR/B ratio in Figures 11b and 14b. In Figure 19b, the [OIII]/[CII] ratio is plotted against the FIR/B ratio. With the exception of irregulars, there does not appear to be a clear trend in [OIII]/[CII] with increasing FIR/B. The irregulars show a decrease in [OIII]/[CII] due to a larger decrease in [CII] than [OIII] emission with increasing FIR/B ratio. The irregulars also have higher [OIII]/[CII] ratios than most spirals as noted by Hunter et al. (2001) and shown in Figure 19. The higher [OIII]/[CII] ratios observed in irregulars are due to stars with higher effective temperatures found in the HII regions of these galaxies that produce doubly ionized [OIII] but little [CII].

6.10 [OIII] 88μm/[OI] 63μm

In Figure 12, the [OI] 63μm emission remains relatively constant when normalized to FIR across a broad range of ISM environments measured by the 60/100μm ratio. The drop seen in [CII] emission is not observed in [OI] 63μm. By comparison, [OIII] 88μm emission showed a weak, increasing trend with increasing 60/100μm ratio in Figure 14a. The [OIII] 88μm/[OI] 63μm ratio is plotted against the 60/100μm ratio in Figure 20a. The [OIII] 88μm/[OI] 63μm ratio has no trend with 60/100μm, unlike [OIII] 88μm/[CII]. In Figures 12b, the [OI] 63μm/FIR ratio showed no trend with FIR/B while the [OIII] 88μm/FIR ratio fell as the FIR/B ratio increased. A slight decline in the [OIII] 88μm/[OI] 63μm ratio is observed as the FIR/B ratio increases and is shown in Figure 20b. Similar to the [OIII] 88μm/[CII] ratio, the [OIII] 88μm/[OI] 63μm ratio for irregulars decreases noticeably with increasing FIR/B. Irregular galaxies also show an elevated [OIII] 88μm/[OI] 63μm ratio when compared to spirals and mentioned by Hunter et al. (2001).

6.11 [OIII] 88μm/[NII]

Both [OIII] 88μm and [NII] 122μm originate in HII regions. The [OIII] 88μm/[NII] ratio is plotted against the 60/100μm and FIR/B ratios in Figure 21 for galaxies unresolved by the LWS. No correlation exists for [OIII] 88μm/[NII] with either the 60/100μm or FIR/B ratios.

7. SUMMARY

I have presented ISOLWS far-infrared line and continuum fluxes for a sample of 227 galaxies selected from the ISO Data Archive spanning an IRAS 60/100μm color range of 0.2-1.4 and 60μm flux densities between 0.1 Jy and 1300 Jy. The far-infrared lines detected in this sample include the seven fine structure lines ([CII] 158μm, [OI] 145μm, [NII] 122μm, [OIII] 88μm, [OI] 63μm, [NIII] 57μm, [OIII] 52μm) and multiple OH (53μm, 65μm, 79μm, 84μm, 119μm, 163μm) and H_2O (59μm, 67μm, 75μm, 101μm, 108μm) transitions. An unidentified line at 74.24μm previously reported in NGC 7027 is detected in NGC 1068. Serendipitous detections of Milky Way [CII] are also observed in twelve sky positions. This sample is the largest collection of FIR line observations ever assembled and includes 465 independent LWS observations (TDTs), 1975 FIR line fluxes and upper limits, and 800 continuum fluxes.

The data presented here can be separated into two subsets, one where the source is resolved and one where it is unresolved by the 75" ISOLWS beam. The resolved subset contains 46 galaxies and the unresolved subset contains 181 galaxies. I have examined statistical trends in the unresolved subset and obtained the following results that may be compared to earlier studies (Malhotra et al. 1997, 2001; Leech et al. 1999; Luhman et al. 1998; Negishi et al. 2001):

1. The LWS continuum agrees with fluxes predicted from the Dale et al. (2001,2002) infrared SED model for galaxies to within 25% at 52μm, 57μm, 63μm, 88μm, 122μm, 145μm, 158μm, and 170μm.
2. The [CII] 158μm/FIR ratio peaks for normal, star-forming galaxies with 60/100μm ratios of 0.3-0.6 and FIR/B ratios of 0.1-1. The [CII]/FIR ratio in quiescent galaxies with 60/100μm ratios less than 0.3 and FIR/B ratios less than 0.1 is consistent with normal, star-forming galaxies. The [CII]/FIR ratio decreases with increasing dust temperatures (60/100μm > 0.6) and star formation activity (FIR/B > 1).
3. The [OI] 63μm/FIR ratio shows no correlation with the 60/100μm and FIR/B ratios.
4. The ratio [NII] 122μm/FIR shows a similar correlation as [CII]/FIR, decreasing as the 60/100μm and FIR/B ratios increase. The [NII]/[CII] shows no correlation with either the 60/100μm or FIR/B ratio, indicating that a large fraction of [CII] may arise from HII regions or that the ratio of PDR to diffuse ionized gas does not vary systematically with 60/100μm or FIR/B.
5. An anticorrelation exists for the [OIII](88μm)/FIR ratio. The [OIII](88μm)/FIR ratio increases as the 60/100μm ratio increases. This increase is due to the larger number of HII regions found in these galaxies. The [OIII] (88μm)/FIR ratio, however, decreases with increasing FIR/B ratio.
6. The [OI] 63μm/[CII] ratio increases as the 60/100μm ratio increases, but shows no correlation with FIR/B. In warmer galaxies (60/100μm > 0.8), [OI] 63μm becomes more important than [CII] in cooling the ISM.
7. The ([OI] 63μm + [CII])/FIR ratio is a measure of the gas heating efficiency, and shows only a slight decrease with increasing 60/100μm ratio for spirals but no decrease for the unresolved galaxies as a whole. The ([OI] 63μm + [CII])/FIR ratio

does, however, decrease with increasing FIR/B ratio for the unresolved subset of galaxies as a whole.

8. The [OIII] 88μm/[CII] ratio increases with increasing 60/100μm ratio. This is due to the dramatic falloff of [CII] emission in warmer, more active galaxies. The [OIII] 88μm/[CII] ratio for irregulars decreases with increasing FIR/B ratio.
9. The [OIII] 88μm/[OI] 63μm ratio has no correlation with the 60/100μm ratio. The [OIII] 88μm/[OI] 63μm ratio decreases slightly with increasing FIR/B.
10. The line ratios of [OI] 145μm/[OI] 63μm and [OIII] 88μm/[NII] show no correlation with either 60/100μm or FIR/B.

These data provide a framework through which the ISM of these galaxies may be studied in the future. These data will soon become available through the ISO Data Archive and NED.

ACKNOWLEDGEMENTS

I thank Harold Corwin for reclassifying the galaxies in this sample according to the RC3 catalog and Danny Dale for the use of his SED model of galaxies to predict the FIR continua of this sample. I have benefited from helpful discussions with Steve Lord, Tom Jarrett, George Helou, and Alessandra Contursi. Finally, I thank Heather Maynard for her suggestions and support. The ISO Spectral Analysis Package (ISAP) is a joint development by the LWS and SWS Instrument Teams and Data Centers. Contributing institutes are CESR, IAS, IPAC, MPE, RAL, and SRON. This research has made use of the NASA/IPAC Extragalactic Database (NED) that is operated by the Jet Propulsion Laboratory, California Institute of Technology, under contract with the National Aeronautics and Space Administration (NASA). This work has made use of data services of the InfraRed Science Archive (IRSA) at the Infrared Processing and Analysis Center/California Institute of Technology, funded by the National Aeronautics and Space Administration (NASA). This work was supported in part by the Jet Propulsion Laboratory, California Institute of Technology, under a contract with NASA.

APPENDIX A. THE EXTENDED SOURCE CORRECTION

The flux calibration of the LWS instrument is based on observations of Uranus, a point source in the LWS aperture. The telescope is diffraction limited at about 110μm, beyond which a fraction of the flux of an on-axis point source may be diffracted out of the aperture. For sources that are extended with respect to the LWS beam, these diffraction losses do not occur. Therefore, an extended source correction must be applied to put these fluxes on a point source calibration scale. In order to apply this correction, the LWS beam of each detector and the telescope PSF must be well known. The extended source correction also assumes that the source is infinitely extended and uniformly bright. None of these galaxies are either, so applying the correction requires great caution. From tests done by the LWS instrument team, the extended source correction works well for sources larger than 3-4' (Gry et al. 2001) when compared to IRAS at 100μm.

The fluxes quoted in Tables 2, 4, and 5 are those which have been measured according to the point source flux calibration. The current understanding of the LWS beam is still not complete, and the extended source correction may change in the future as more work is done. Therefore, the extended source correction has not been applied to the line fluxes listed in this paper, but those galaxies that may require an extended source correction have been noted in Tables 2, 4, and 5. The most up to date effective apertures and corrections are listed in Table 7, taken from the ISOLWS Handbook IV (Gry et al. 2001).

APPENDIX B. LWS CONTINUUM COMPARISON WITH IRAS DATA

An extensive comparison of the LWS continuum fluxes and IRAS catalog fluxes was done for galaxies unresolved by the LWS. The following criteria were applied to this study: 1)galaxies must have an IRAS Point-Source Catalog (PSC) detection, 2)galaxies' FIR emission is concentrated within the 75" LWS beam and 3)LWS data must exist in the vicinity of 60μm and 100μm wavelengths to be used for a continuum estimation. Using these three criteria, 41 galaxies were observed in the L01 AOT and 104 in the L02 AOT.

For L01 observations, the 60μm and 100μm continuum were estimated by performing synthetic photometry with an algorithm provided in ISAP. This photometry is performed on the spectra by integrating across the IRAS passbands. The 60μm and 100μm flux densities are determined using the IRAS assumption that the source SED shape is of the form λf_λ = constant. For the comparison at 60μm a correction must be introduced because the LWS does not cover the entire IRAS 60μm filter (43-197μm vs. 27-87μm). The galaxies used for this comparison span a wide range of 60/100μm ratios (0.2-1.4), thus, the amount of the integrated flux in the IRAS 60μm filter missed by the LWS varies depending on the SED shape of the galaxy. Dale et al. (2001, 2002) describe a sequence of galaxy SED models sorted across a range of 60/100μm ratios. Using these SED models, the amount of the total integrated flux in the IRAS 60μm filter missed by the LWS between 27μm and 43μm varies from 3% to 7% for these 60/100μm ratios. This correction based on the 60/100μm ratio of the galaxy is applied to the LWS 60μm fluxes derived from L01 observations.

For L02 observations, synthetic photometry cannot be used because the sparse sampling creates gaps in the spectra. Instead, a monochromatic flux is estimated by fitting a linear baseline to a 2-5μm slice of spectra surrounding the wavelengths 60μm and 100μm. After the correction to the 60μm LWS fluxes for the amount of IRAS flux missed by the LWS, the L02 60μm and 100μm monochromatic continuum fluxes must also have a secondary correction applied because these monochromatic fluxes cannot be directly compared to the IRAS fluxes. Since the fluxes derived from the L02 observations were taken by fitting a linear baseline through the IRAS filter central wavelengths, the assumption would be that the flux at these wavelengths is equal to the flux over the entire IRAS passband for galaxies of these 60/100μm colors. A calculation of the difference between the monochromatic fluxes, estimated by fitting a linear baseline to the spectra at 60μm and 100μm, and the synthetic photometry fluxes from integrating over the IRAS filters was done using a set of pointed observations in which the same sky

position on a galaxy was observed in both the L01 and L02 AOTs. The monochromatic fluxes overestimate the integrated spectral photometry on average by 11% at 60μm and 9% at 100μm. I correct the monochromatic L02 fluxes for these overestimations from using linear fits to the spectra.

After these two corrections were applied, the background was estimated using IRSKY and then removed from the LWS data. Figure 22 shows how the LWS and IRAS data compare. The LWS error bars are a combination of the errors associated with the baseline fit to the line and the pipeline calibration errors. The IRAS error bars are taken directly from the PSC as given by NED. The LWS fluxes are, on average, 1% lower and 2% higher than IRAS at 60μm and 100μm, respectively, for IRAS fluxes above 10 Jy, a remarkable agreement. Below 10 Jy, the dispersion increases from 20% to 50%, not surprising since the dark current is comparable to 10 Jy for these sources. Both the L01 and L02 continuum fluxes show similar offsets and dispersions in the LWS-IRAS comparison.

APPENDIX C. 170μm CONTINUUM COMPARISON WITH ISOPHOT DATA

The continuum at 170μm falls off by a factor of 2 or more compared to the blackbody peaks of these galaxies between 40μm and 60μm. For galaxies with 60μm fluxes less than 10 Jy, the detection limit of the LWS may be reached, and the reliability of the 170μm continuum is once again subject to uncertainties in the dark current. Using published fluxes from ISOPHOT pointed observations at 180μm (Klaas et al. 2001) and 170μm Serendipity Survey (Stickel et al. 2000), 25 galaxies constrained to the LWS beam are compared to 170μm fluxes measured by the LWS.

Both ISOPHOT studies utilized the broad C_160 filter; therefore, two corrections must be applied to the LWS monochromatic fluxes. These monochromatic fluxes are compared to 170μm fluxes derived by integrating over the ISOPHOT C_160 filter using the synthetic photometry algorithm in ISAP. On average, the monochromatic LWS fluxes are 11% higher than equivalent synthetic photometry fluxes, and this correction is applied to the LWS monochromatic fluxes. The second correction applied adjusts for the difference in wavelength spanned by the LWS and ISOPHOT C_160 filter (43-197μm vs. 100-240μm). The flux missed by the LWS in the ISOPHOT filter depends upon the SED shape of the galaxy, and this flux is estimated by assuming the Dale et al. (2001) SED shape of a galaxy for a given 60/100μm ratio. Typically, this correction is approximately 3% for the range of 60/100μm ratios of these galaxies.

The total correction applied to LWS fluxes is approximately 14%, and Figure 23 is the resulting plot of this comparison. The ISOPHOT and LWS fluxes track each other well between 1 Jy and 100 Jy although the dispersion increases significantly below 10 Jy. This effect is due to the large uncertainties in the dark current at this wavelength and flux regime. Considering the differences in beam size and calibration between the LWS and ISOPHOT instruments, the 30% overall agreement is similar to the uncertainties of the two instruments at this wavelength.

REFERENCES

Bennett, C.L., Fixsen, D.J., Hinshaw, G., Mather, J.C., Moseley, S.H., Wright, E.L., Eplee, R.E., Gales, J., Hewagama, T., Isaacman, R.B., Shafer, R.A., Turpie, K. 1994, ApJ, 434, 587

Bock, J.J., Hristov, V.V., Kawada, M., Matsuhara, H., Matsumoto, T., Matsuura, S., Mauskopf, P.D., Richards, P.L., Tanaka, M., Lange, A.E. 1993, ApJ, 410, L115

Boggess, N.W., Mather, J.C., Weiss, R., Bennett, C.L., Cheng, E.S., Dwek, E., Gulkis, S., Hauser, M.G., Janssen, M.A., Kelsall, T., Meyer, S.S., Moseley, S.H., Murdock, T.L., Shafer, R.A., Silverberg, R.F., Smoot, G.F., Wilkinson, D.T., Wright, E.L. 1992, ApJ, 397, 420

Boreiko, R.T., Betz, A.L. 1997, ApJS, 111, 409

Boulanger, F., Beichman, C., Desert, F.X., Helou, G., Perault, M., Ryter, C. 1988, ApJ, 332, 328

Bradford, C.M., Stacey, G.J., Fischer, J.A., Smith, H.A., Cohen, R.J., Greenhouse, M.A., Lord, S.D., Lutz, D., Maiolino, R., Malkan, M.A., Rieu, N. 1999, in "The Universe as Seen by ISO", ed. Cox, P. & Kessler, M.F., ESA SP-427 (Noordwijk, Netherlands), 861

Carral, P., Hollenbach, D.J., Lord, S.D., Colgan, S.W.J., Haas, M.R., Rubin, R.H., Erickson, E.F. 1994, ApJ, 423, 223

Colbert J.W., Malkan, M.A., Clegg, P.E., Cox, P., Fischer, J., Lord, S.D., Luhman, M., Satyapal, S., Smith, H.A., Spinoglio, L., Stacey, G., & Unger, S.J. 1999, ApJ, 511, 721

Clegg, P. et al. 1996, A&A, 315, L38

Colgan, S.W.J., Haas, M.R., Erickson, E.F., Rubin, R.H., Simpson, J.P., Russell, R.W. 1993, ApJ, 413, 237

Contursi, A., Kaufman, M.J., Helou, G., Hollenbach, D.J., Brauher, J.R., Stacey, G.J., Dale, D.A., Malhotra, S., Rubio, M., Rubin, R.H., Lord, S.D., submitted to ApJ

Crawford, M.K., Genzel, R., Townes, C.H., Watson, D.M. 1985, ApJ, 291, 755

Dale, D., Silbermann, N.A., Helou, G., et al. 2000, ApJ, 120, 583

Dale, D.A., Helou, G., Contursi, A., Silbermann, N.A., Kolhatkar, S. 2001, ApJ, 549, 215

Dale, D.A., Helou, G., Brauher, J.R., et al. 2002, in preparation

de Vaucouleurs, G., de Vaucouleurs, A., Corwin, H.G., Buta, R.J., Paturel, G., & Fouque, P. 1991, Third Reference Catalogue of Bright Galaxies (New York: Springer)

Duffy, P.B., Erickson, E.F., Haas, M.R., Houck, J.R. 1987, ApJ, 315, 68

Fischer, J., Lord, S.D., Unger, S.J., Bradford, C.M., Brauher, J.R., Clegg, P.E., Colbert, J.W., Cox, P., Greenhouse, M.A., Harvey, V., Malkan, M.A., Melnick, G., Smith, H.A., Spinoglio, L., Strelnitski, V., Suter, J.-P. 1999, in "The Universe as Seen by ISO", ed. Cox, P. & Kessler, M.F., ESA SP-427 (Noordwijk, Netherlands), 817

Gry, C., Swinyard, B., Harwood, A., Trams, N., Leeks, S., Lim, T., Sidher, S., Lloyd, C., Pezzuto, S., Molinari, S., Lorente, S., Caux, E., Chan, J., Hutchinson, G., Burgdorf, M. 2000, LWS Handbook IV, version 1.2

Hartmann, D., & Burton, W.B. 1997, Atlas of Galactic Neutral Hydrogen (Cambridge: Cambridge University Press)

Harvey, V.I., Satyapal, S., Luhman, M.L., Fischer, J., Clegg, P.E., Cox, P., Greenhouse, M.A., Lord, S.D., Malkan, M.A., Smith, H.A., Spinoglio, L., Stacey, G.J., Unger, S.J. 1999, in "The Universe as Seen by ISO", ed. Cox, P. & Kessler, M.F., ESA SP-427 (Noordwijk, Netherlands), 889

Heiles, C. 1994, ApJ, 436, 720

Helou, G. 1986, ApJ, 311, L33

Helou, G., Khan, I.R., Malek, L., Boehmer, L. 1988, ApJS, 68, 151

Helou, G., Malhotra, S., Beichman, C.A., Dinerstein, H., Hollenbach, D.J., Hunter, D.A., Lo, K.Y., Lord, S.D., Lu, N.Y., Rubin, R.H., Stacey, G.J., Thronson, H.A., Jr., Werner, M.W. 1996, A&A, 315, L157

Hollenbach, D.J., Takahashi, T., Tielens, A.G.G.M. 1991, ApJ, 377, 192

Hollenbach, D.J., Tielens, A.G.G.M. 1997, ARA&A, 35, 179

Hunter, D.A., Kaufman, M., Hollenbach, D.J., Rubin, R.H., Malhotra, S., Dale, D.A., Brauher, J.R., Silbermann, N.A., Helou, G., Contursi, A., Lord, S.D. 2001, ApJ, 553, 121

Hutchinson, M.G., Chan, S.J., Sidher, S.D. 2001, in "The Calibrations Legacy of the ISO Mission", ed. Metcalfe, L. & Kessler, M.F., ESA SP-481

Kaufman, M.J., Wolfire, M.G., Hollenbach, D.J., Luhman, M.L. 1999, ApJ, 527, 795

Kessler, M.F. et al. 1996, A&A, 315, L27

Leech, K.J., Völk, Heinrichsen, I., Hippelein, H., Metcalfe, L., Pierini, D., Popescu, C.C., Tuffs, R.J., & Xu, C. 1999, MNRAS, 310, 317

Liu, X.-W., Barlow, M.J., Rieu, N.-Q., et al. 1996, A&A, 315, L257

Lord, S.D. Hollenbach, D.J., Haas, M.R., Rubin, R.H., Colgan, S.W.J., Erickson, E.F. 1996, ApJ, 465, 703

Luhman, M.L., Satyapal. S., Fischer, J., Wolfire, M.G., Cox, P., Lord, S.D., Smith, H.A., Stacey, G.J., & Unger, S.J. 1998, ApJ, 504, L11

Madden, S.C., Geis, N., Genzel, R., Herrmann, F., Jackson, J., Poglitsch, A., Stacey, G.J., Townes, C.H. 1993, ApJ, 407, 579

Madden, S.C., Poglitsch, A., Geis, N., Stacey, G.J., Townes, C.H. 1997, ApJ, 483, 200

Malhotra, S., Helou, G., Stacey, G., Hollenbach, D., Lord, S., Beichman, C.A., Dinerstein, H., Hunter, D.A., Lo, K.Y., Lu, N.Y., Rubin, R.H., Silbermann, N., Thronson Jr., H.A., & Werner, M.W. 1997, ApJ, 491, L27

Malhotra, S., Hollenbach, D., Helou, G., Silbermann, N., Valjavec, E., Rubin, R.H., Dale, D., Hunter, D., Lu, N., Lord, S., Dinerstein, H., Thronson, H. 2000, ApJ, 543, 634

Malhotra, S., Kaufman, M., Hollenbach, D., Helou, G., Rubin, R.H., Brauher, J., Dale, D., Lu, N.Y., Lord, S., Stacey, G., Contursi, A., Hunter, D.A., Dinerstein, H. 2001, ApJ, 561, 766

Nakagawa, T., Doi, Y., Yui, Y.Y., Okuda, H., Mochizuki, K., Shibai, H., Nishimura, T., Low, F.J. 1995, ApJ, 455, L35

Negishi, T., Onaka, T., Chan, K.-W., Roellig, T.L., 2001, A&A, 375, 566

Oliva, E., Moorwood, A.F.M., Drapatz, S., Lutz, D., Sturm, E. 1999, A&A, 343, 943

Petuchowski, S.J., Bennett, C.L. 1993, ApJ, 405, 591

Pierini, D., Leech, K.J., Tuffs, R.J., & Völk, H.J. 1999, MNRAS, 303, L29

Reach, W.T., Wall, W.F., Odegard, N. 1998, ApJ, 507, 507

Rubin, R.H. 1985, ApJS, 57, 349

Rubin, R.H., Simpson, J.P., Lord, S.D., Colgan, S.W.J., Erickson, E.F., Haas, M.R. 1994, ApJ, 420, 772

Sauty, S., Gerin, M., Casoli, F. 1998, A&A, 339, 19

Shibai, H., Okuda, H., Nakagawa, T., Matsuhara, H., Maihara, T., Mizutani, K., Kobayashi, Y., Hiromoto, N. 1991, ApJ, 374, 522

Skinner, C.J., Smith, H.A., Sturm, E., Barlow, M.J., Cohen, R.J., Stacey, G.J. 1997, Nature, 386, 472

Spinoglio, L., Suter, J.-P., Malkan, M.A., Clegg, P.E., Fischer, J., Greenhouse, M., Smith, H.A., Pequignot, D., Stacey, G.J., Rieu, N., Unger, S.J., Strelnitski, V. 1999, in "The Universe as Seen by ISO", ed. Cox, P. & Kessler, M.F., ESA SP-427 (Noordwijk, Netherlands), 969

Sturm, E., Bauer, O.H., Brauher, J., Buckley, M., Harwood, A., Helou, G., Khan, I., Li, J., Lord, S., Lutz, D., Mazzarella, J., Morris, P.W., Narron, B., Sidher, S., Swinyard, B., Unger, S.J., Verstraete, L., Vivares, F., Wieprecht, E., & Wiezorrek, E. 1998, ADASS, 7, 161

Stacey, G.J., Geis, N., Genzel, R., Lugten, J.B., Poglitsch, A., Sternberg, A., & Townes, C.H. 1991, ApJ, 373, 423

Stickel, M., Lemke, D., Klaas, U., Beichman, C.A., Rowan-Robinson, M., Efstathiou, A., Bogun, S., Kessler, M.F., Richter, G. 2000, A&A, 359, 865

Swinyard, B.M., Burgdorf, M.J., Clegg, P.E., Davis, G.R., Griffin, M.J., Gry, C., Leeks, S.J., Lim, T.L., Pezzuto, S., Tommasi, E. 1998, SPIE, 3354, 888

Tielens, A.G.G.M., Hollenbach, D. 1985, ApJ, 291, 722

Wolfire, M.G., Tielens, A.G.G.M., Hollenbach, D. 1990, ApJ, 358, 116

Wright, E.L., Mather, J.C., Bennett, C.L. et al. 1991, ApJ, 381, 200

Figure Legends

Fig 1 – Aitoff projection of the galaxies selected for this sample. The galaxies in this sample are distributed across the sky. Galaxies unresolved by the LWS in the FIR are displayed with crosses. Resolved galaxies by the LWS in the FIR are shown with open squares. The clump of galaxies at RA, Dec (70°, 280°) are members of the Virgo Cluster.

Fig 2 – Histogram of the distribution of the RC3 morphologies of the resolved and unresolved subsets of galaxies. The resolved subset is cross-shaded and the unresolved is clear.

Fig 3 – Histogram of the distribution of redshifts for the resolved and unresolved subsets. The resolved galaxy redshifts are cross-shaded and the unresolved are clear.

Fig 4 – Histogram of the distribution of measured IRAS 60μm and 100μm flux densities. The resolved galaxy subset fluxes are cross-shaded and the unresolved are clear.

Fig 5 – Histogram of the distribution of the IRAS 60/100μm ratio and FIR. The resolved galaxy subset is cross-shaded and the unresolved subset is clear.

Fig 6 – The IRAS color-color diagram for the galaxies in this sample. Quiescent galaxies are located towards the upper left and active galaxies towards the lower right. Filled circles are galaxies in the unresolved subset. Open circles are galaxies in the resolved subset.

Fig 7 – Two example LWS spectra representing the pipeline product L01 and L02 AOTs displayed before and after using the LIA and ISAP reduction. Improvements from using LIA and ISAP include not only the removal of fringes and glitch removal but also the reduction of negative continuum fluxes and misaligned adjacent detectors.

Fig 8 – Comparison of the LWS continuum fluxes of galaxies unresolved by the LWS beam and the Dale et al. (2001) SED model prediction for eight FIR wavelengths. Open triangles represent continuum fluxes taken from a fully sampled L01 spectrum. Open circles represent continuum fluxes taken from a sparsely sampled L02 line spectrum. The dashed line is the one-to-one correlation.

Fig 9 – Examples of the [CII](158μm) line found in this sample. This figure is a representative selection of some varying signal-to-noise detections and shows how well a Gaussian with the effective instrumental width fits the line data. Error bars are taken from the uncertainty in the averaging of the spectral scans in each bin.

Fig 10 – Three LWS spectra with both Milky Way [CII](158μm) and [CII] at the redshift of the observed galaxy is plotted along with the corresponding $1^{\circ}\times1^{\circ}$ IRAS 100μm images. The LWS observation for each galaxy was located at the center of each IRAS image. The line through the spectra is a best fit using a linear baseline and two instrumental width Gaussians.

Fig 11 – The ratio of [CII](158μm) to far-infrared continuum, [CII](158μm)/FIR, is plotted against the IRAS 60/100μm and FIR/B ratios for galaxies unresolved by the LWS. Spirals (RC3=0-9) are plotted as open circles. Lenticulars (RC3=-3,-2) are plotted as open diamonds. Ellipticals (RC3=-6,-5,-4) are plotted as open squares. Irregulars (RC3=10,11,90) are plotted as open stars. Peculiars (RC3=99) are plotted as open triangles. Galaxies without an RC3 classification are plotted as asterisks. The line fluxes are uncertain by about 20%. Galaxies with no [CII] detection are shown as 3σ upper limits in the figure. The data are separated into sub-bins of 60/100μm and FIR/B. The dashed lines show the bins. The median in each bin of [CII]/FIR for 3σ or higher detections of [CII] are shown as horizontal lines. Regardless of morphology, the [CII](158μm)/FIR ratio decreases as the 60/100μm and FIR/B ratios increase.

Fig 12 – The ratio of [OI](63μm) to far-infrared continuum, [OI](63μm)/FIR, is plotted against the IRAS 60/100μm and FIR/B ratios for galaxies unresolved by the LWS. The [OI](63μm)/FIR shows no trends with either 60/100μm or FIR/B. The symbols are the same as Figure 11. The line fluxes are uncertain by about 20%. Galaxies with no [OI](63μm) detection are shown as 3σ upper limits in the figure.

Fig 13 – The ratio of [NII](122μm) to far-infrared continuum, [NII](122μm)/FIR, is plotted against the IRAS 60/100μm and FIR/B ratios for galaxies unresolved by the LWS. The [NII](122μm)/FIR ratio decreases as the 60/100μm and FIR/B ratios increase, similar to the behavior to the [CII] line. The symbols are the same as Figure 11. The line fluxes are uncertain by about 20%. Galaxies with no [NII] detection are shown as 3σ upper limits in the figure.

Fig 14 – The ratio of [OIII](88μm) to far-infrared continuum, [OIII](88μm)/FIR, is plotted against the IRAS 60/100μm and FIR/B ratios for galaxies unresolved by the LWS. The [OIII](88μm)/FIR ratio increases with increasing 60/100μm ratio and decreases with increasing FIR/B ratio. The symbols are the same as Figure 11. The line fluxes are uncertain by about 20%. Galaxies with no [OIII](88μm) detection are shown as 3σ upper limits in the figure.

Fig 15 – The ratio of [OI](63μm)/[CII](158μm) is plotted against the IRAS 60/100μm and FIR/B ratios for galaxies unresolved by the LWS. The [OI](63μm)/[CII](158μm) ratio increases as the 60/100μm ratio increases, but shows no correlation with the FIR/B ratio. The symbols are the same as Figure 11. The error bar represents a 20% error in the ratio. Galaxies with no [OI](63μm) detection are shown as 3σ upper limits in the figure.

Fig 16 – The ratio of [NII](122μm)/CII](158μm) is plotted against the IRAS 60/100μm and FIR/B ratios for galaxies unresolved by the LWS. The symbols are the same as Figure 11. The error bar represents a 20% error in the ratio. Galaxies with no [NII](122μm) detection are shown as 3σ upper limits in the figure.

Fig 17 – The ratio of [OI](145μm)/[OI](63μm) is plotted against the IRAS 60/100μm and FIR/B ratios for galaxies unresolved by the LWS. The symbols are the same as Figure 11. The error bar represents a 20% error in the ratio. Galaxies with no [OI](145μm) detection are shown as 3σ upper limits in the figure.

Fig 18 – The ratio of ([OI](63μm) + [CII](158μm))/FIR is plotted against the IRAS 60/100μm and FIR/B ratios for galaxies unresolved by the LWS. The symbols are the same as Figure 11. The error bar represents a 20% error in the ratio. Galaxies with [CII] but no [OI](63μm) detection are shown as 3σ upper limits in the figure.

Fig 19 – The ratio of [OIII](88μm)/[CII](158μm) is plotted against the IRAS 60/100μm and FIR/B ratios for galaxies unresolved by the LWS. The [OIII](88μm)/[CII](158μm) ratio increases with increasing 60/100mm ratio, but shows no correlation with FIR/B.

The symbols are the same as Figure 11. The error bar represents a 20% error in the ratio. Galaxies with no [OIII](88μm) detection are shown as 3σ upper limits in the figure.

Fig 20 – The ratio of [OIII](88μm)/[OI](63μm) is plotted against the IRAS 60/100μm and FIR/B ratios for galaxies unresolved by the LWS. Galaxies with no [OIII](88μm) detection are shown as 3σ upper limits in the figure. Galaxies with no [OI](63μm) detection are shown as 3σ lower limits in the figure. The symbols are the same as Figure 11. The error bar represents a 20% error in the ratio.

Fig 21 – The ratio of [OIII](88μm)/[NII](122μm) is plotted against the IRAS 60/100μm and FIR/B ratios for galaxies unresolved by the LWS. Galaxies with no [OIII](88μm) detection are shown as 3σ upper limits in the figure. Galaxies with no [NII](122μm) detection are shown as 3σ lower limits in the figure. The symbols are the same as Figure 11. The error bar represents a 20% error in the ratio.

Fig 22 – Comparison of LWS continuum fluxes to the IRAS fluxes at 60μm and 100μm. Open triangles are continuum fluxes from L01 observations. Open circles are continuum fluxes from L02 observations. A typical error bar is plotted in the lower right of each plot. The LWS error bar is calculated from the combination of the systematic and measured flux errors and represents an average 20% error. The IRAS flux error is taken from the IRAS Point Source Catalog (PSC) and represents an average 10% error. The dashed line is the one-to-one correlation.

Fig 23 – Comparison of LWS continuum fluxes to ISOPHOT Serendipity Survey fluxes (Stickel et al. 2000) at 170μm for galaxies unresolved by the LWS. Filled circles are measurements from L01 observations and open triangles are from L02 observations. The ISOPHOT errors represent 40% calibration uncertainties quoted by Stickel et al. (2000) and the LWS errors represent 30% calibration uncertainties at 170μm. The dashed line is the one-to-one correlation.

Fig. 1

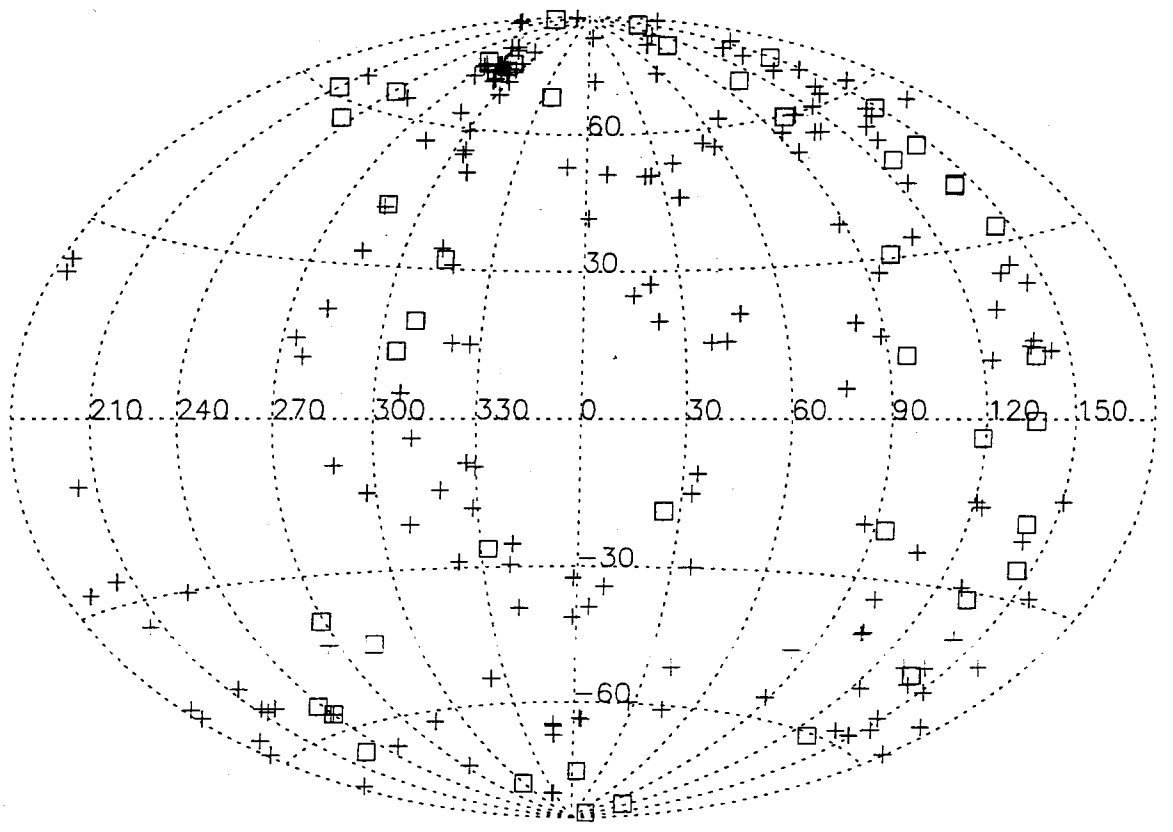

Fig. 2

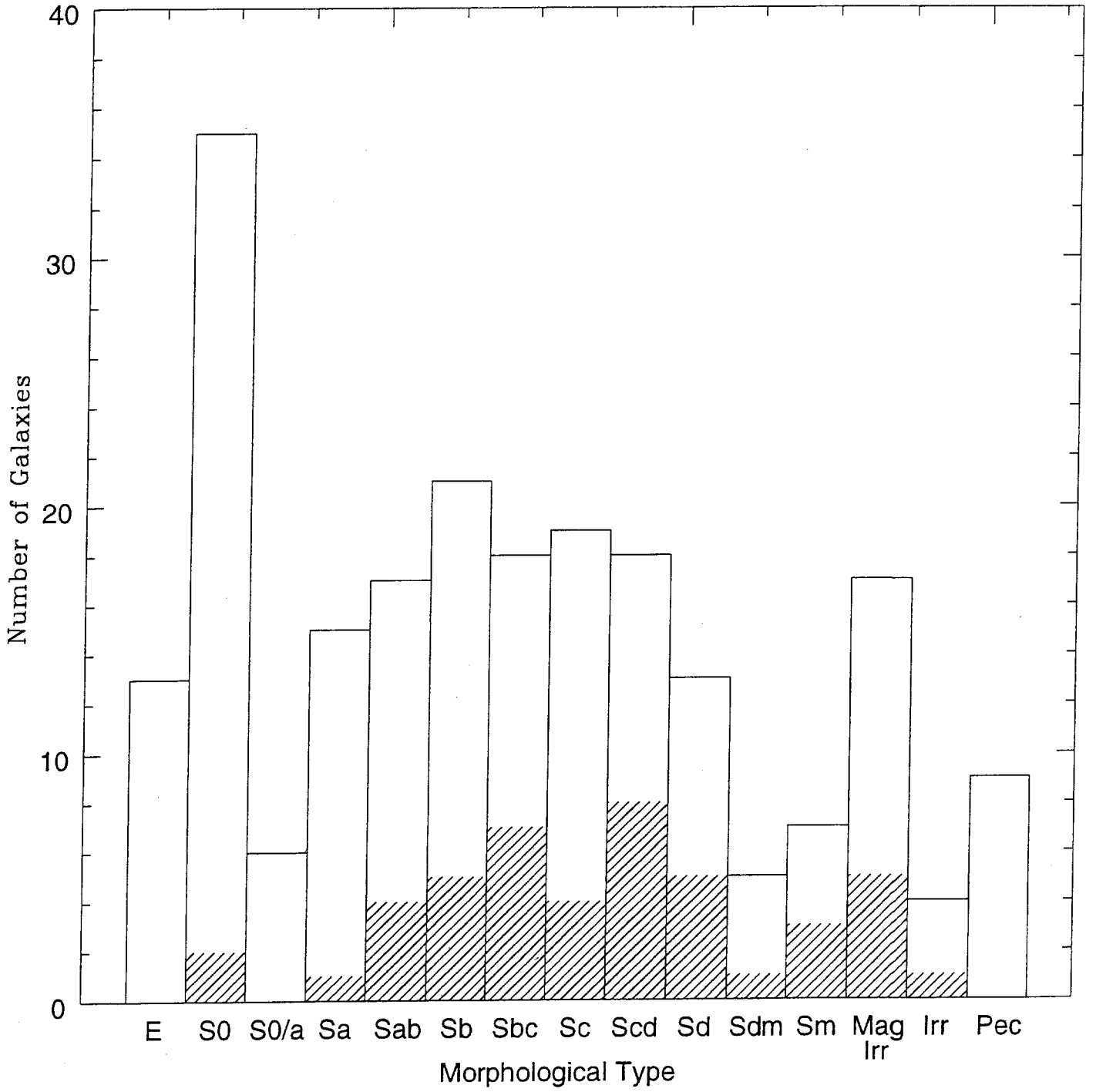
40
30
20
10
0
Number of Galaxies
E
S0
S0/a
Sa
Sab
Sb
Sbc
Sc
Scd
Sd
Sdm
Sm
Mag Irr
Irr
Pec
Morphological Type

Fig. 3

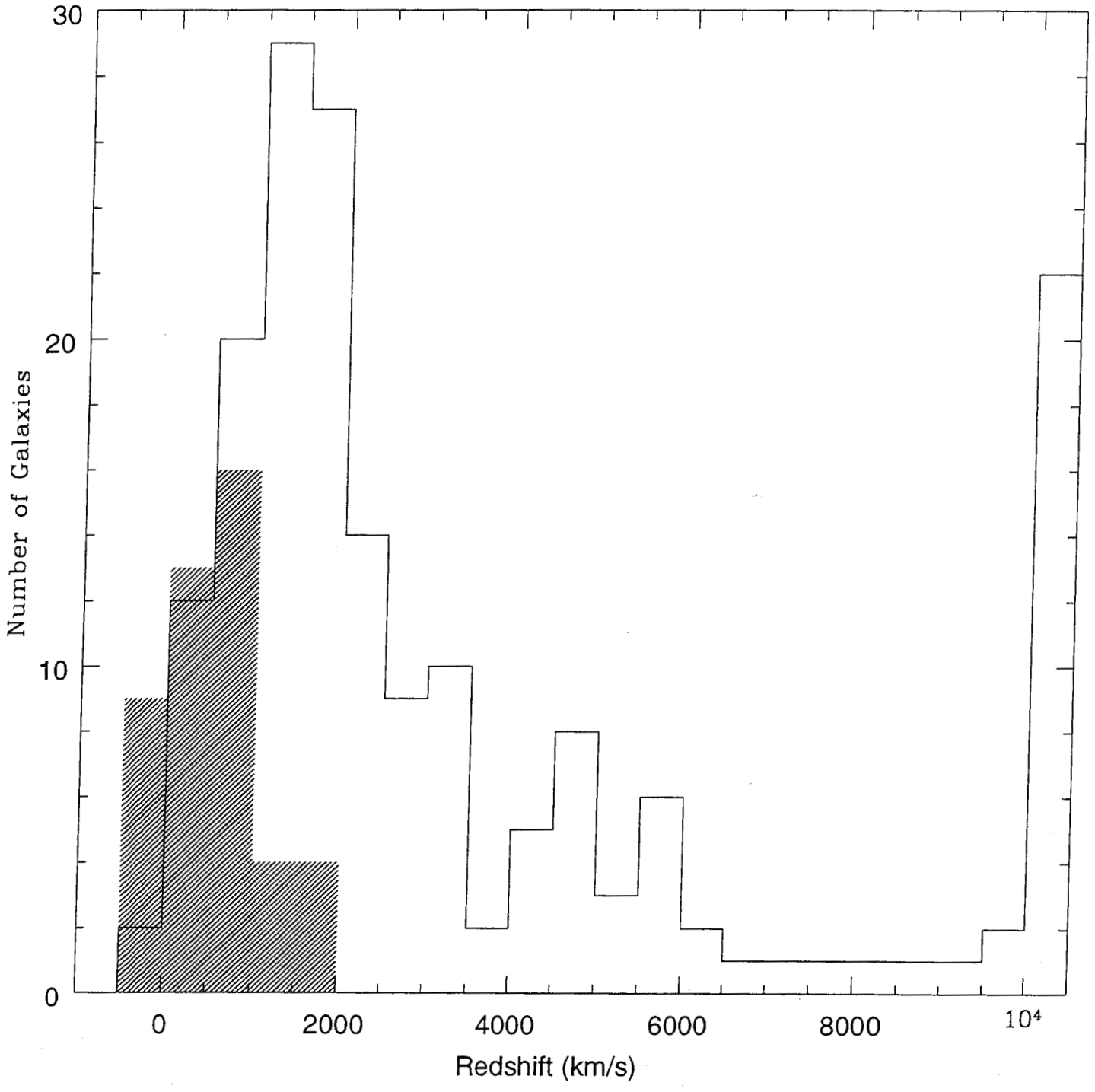
30
20
10
0
Number of Galaxies
0
2000
4000
6000
8000
10⁴
Redshift (km/s)

Fig. 4

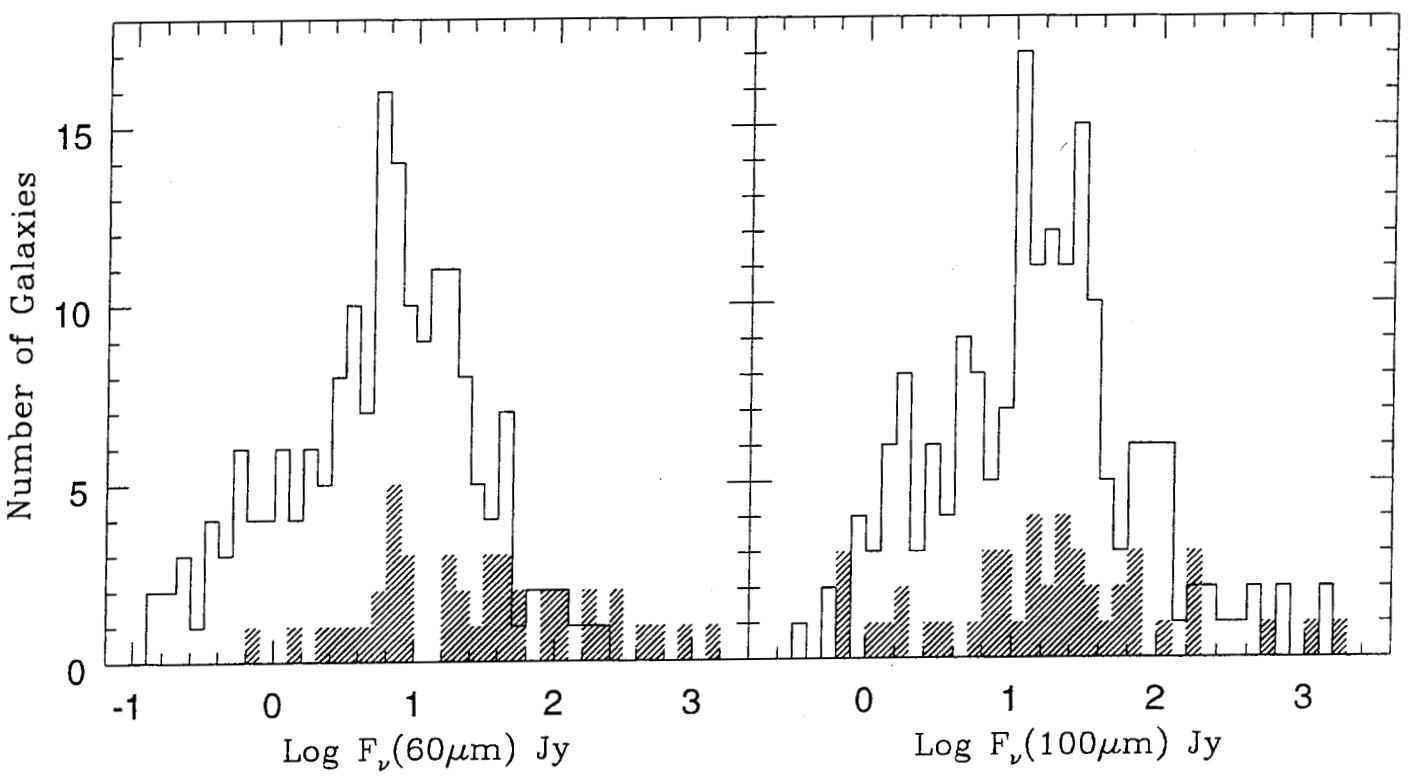
Number of Galaxies
0
5
10
15
-1
0
1
2
3
Log $F_\nu(60\mu m)$ Jy
0
1
2
3
Log $F_\nu(100\mu m)$ Jy

Fig. 5

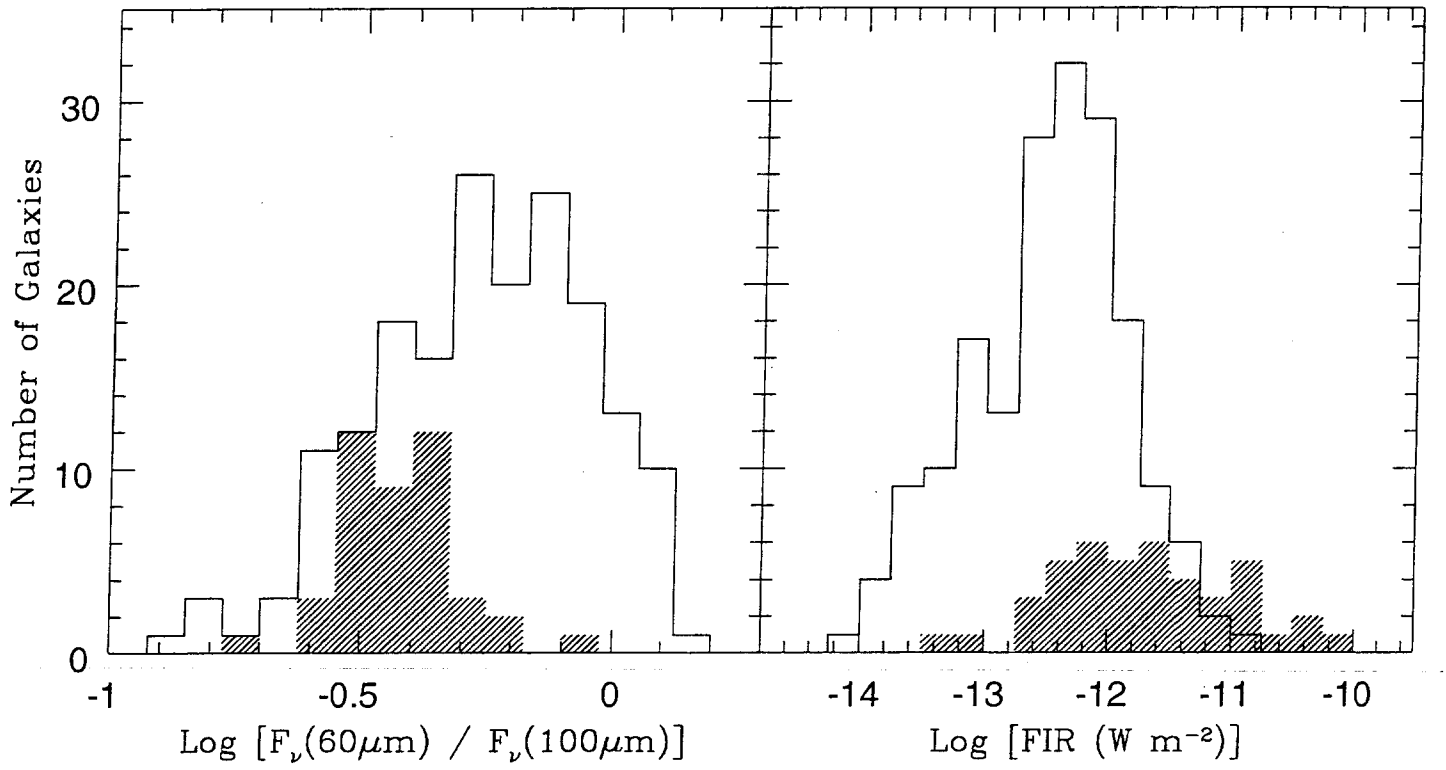
Number of Galaxies
30
20
10
0
-1
-0.5
0
Log [$F_\nu(60\mu m)$ / $F_\nu(100\mu m)$]
-14
-13
-12
-11
-10
Log [FIR (W m^{-2})]

Fig. 6

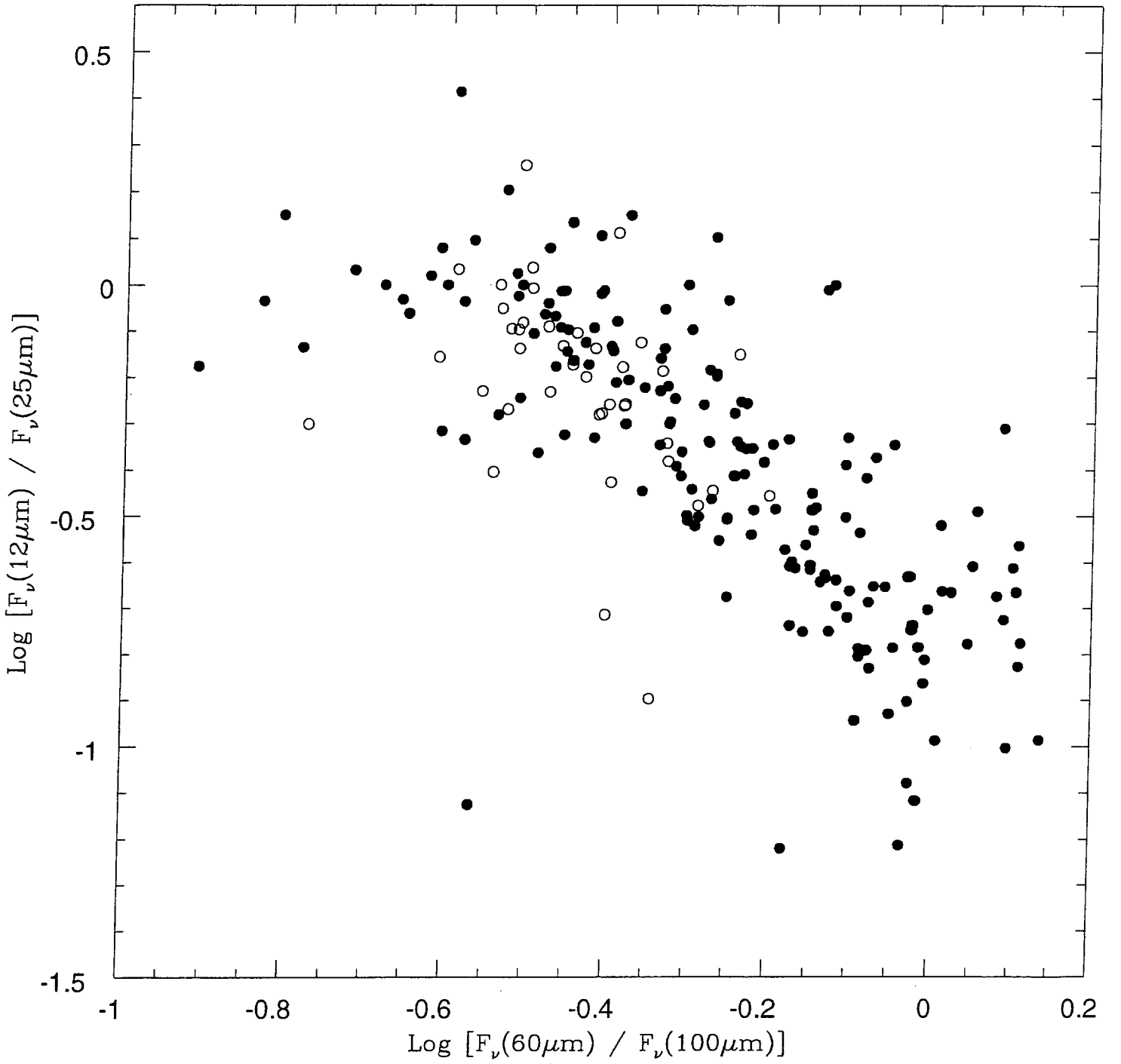
0.5
0
-0.5
-1
-1.5
-1
-0.8
-0.6
-0.4
-0.2
0
0.2
Log [$F_\nu(12\mu m)$ / $F_\nu(25\mu m)$]
Log [$F_\nu(60\mu m)$ / $F_\nu(100\mu m)$]

Fig. 7

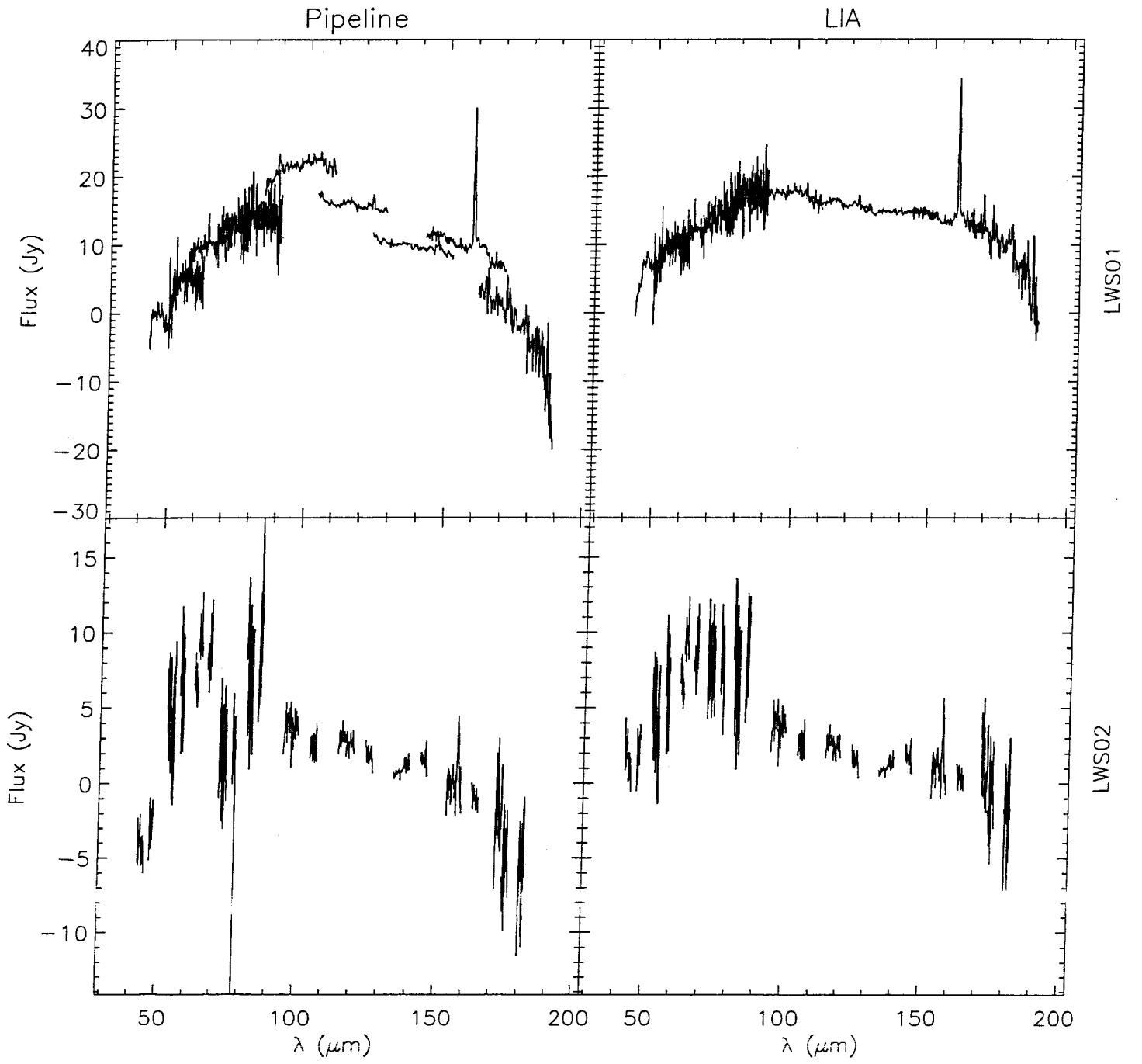
Pipeline
LIA
LWS01
LWS02
Flux (Jy)
Flux (Jy)
λ (μm)
λ (μm)
40
30
20
10
0
−10
−20
−30
15
10
5
0
−5
−10
50
100
150
200

Fig. 8

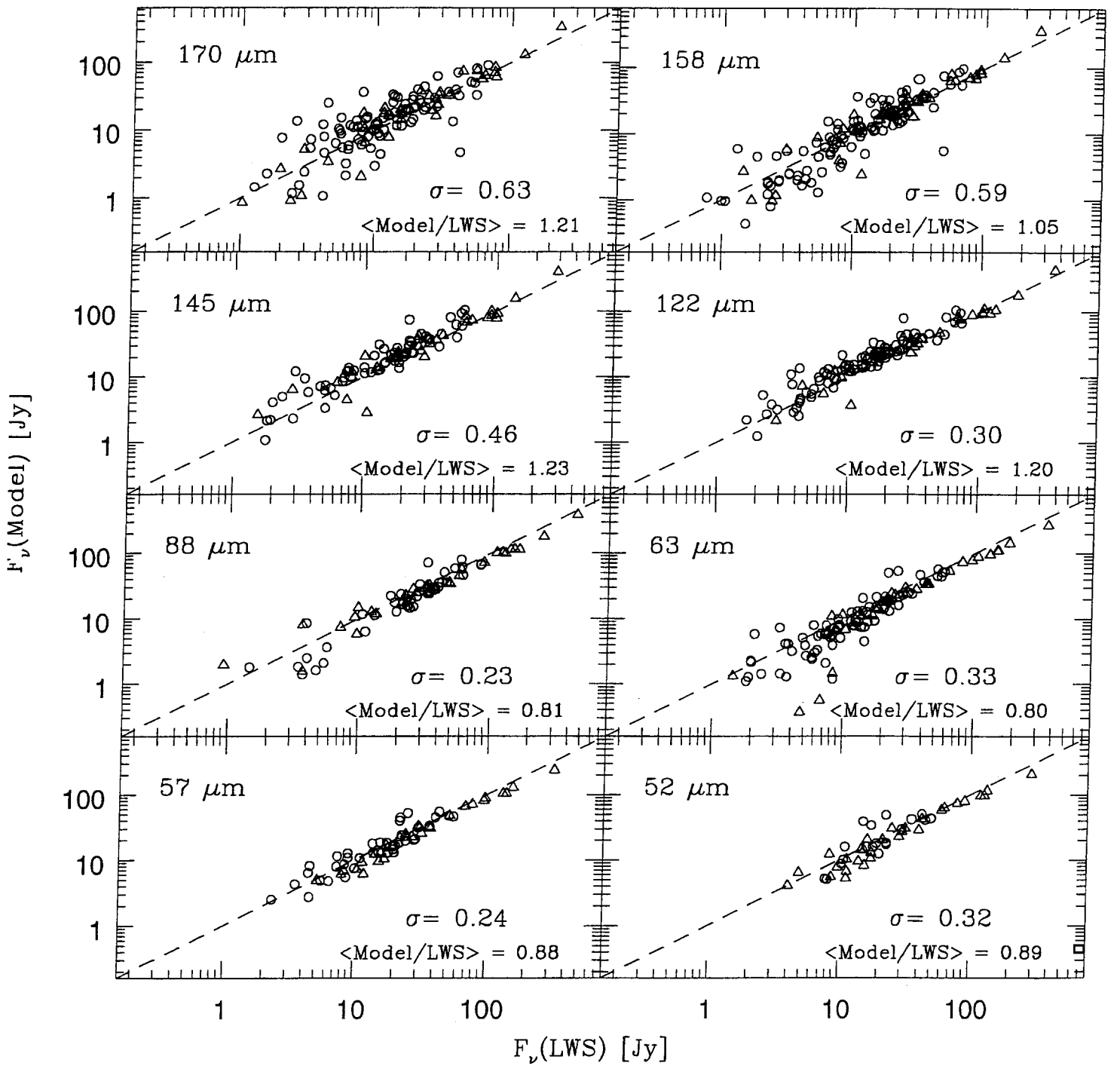
170 μm
σ= 0.63
<Model/LWS> = 1.21
158 μm
σ= 0.59
<Model/LWS> = 1.05
145 μm
σ= 0.46
<Model/LWS> = 1.23
122 μm
σ= 0.30
<Model/LWS> = 1.20
88 μm
σ= 0.23
<Model/LWS> = 0.81
63 μm
σ= 0.33
<Model/LWS> = 0.80
57 μm
σ= 0.24
<Model/LWS> = 0.88
52 μm
σ= 0.32
<Model/LWS> = 0.89
100
10
1
1
10
100
F_ν(Model) [Jy]
F_ν(LWS) [Jy]

Fig. 9

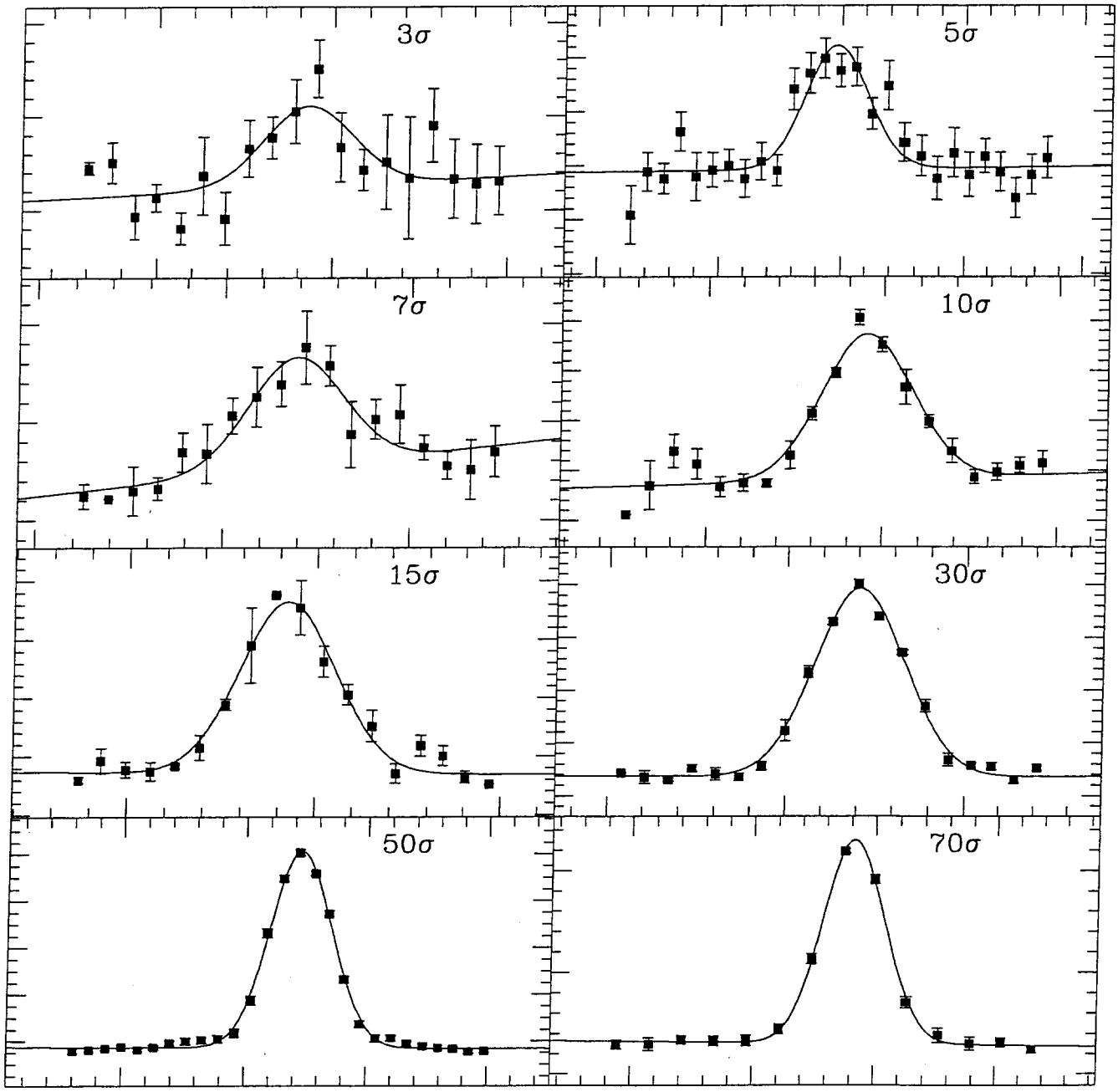

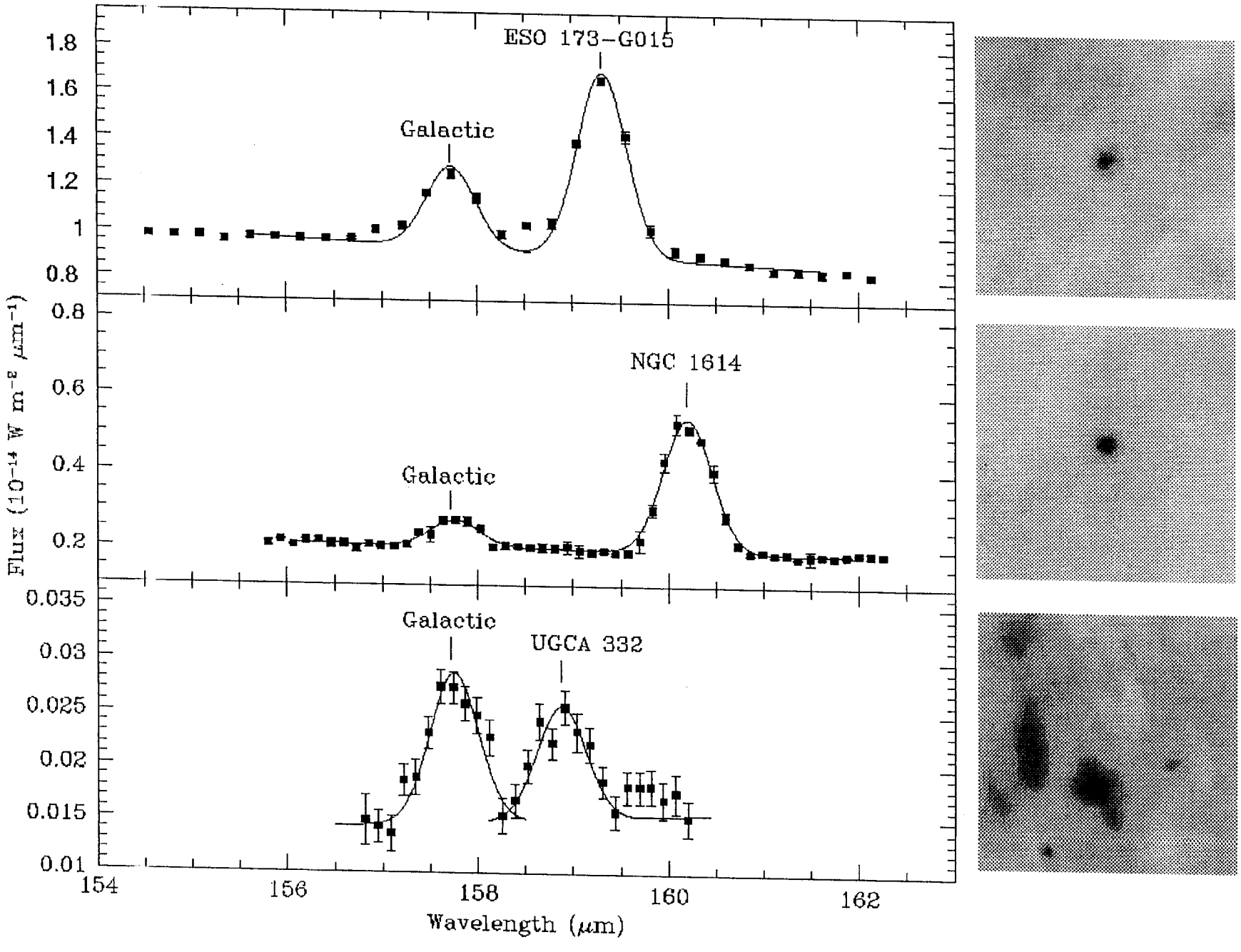
ESO 173-G015
Galactic
NGC 1614
Galactic
Galactic
UGCA 332
Flux (10^{-14} W m^{-2} μm^{-1})
Wavelength (μm)
1.8
1.6
1.4
1.2
1
0.8
0.8
0.6
0.4
0.2
0.035
0.03
0.025
0.02
0.015
0.01
154
156
158
160
162

Fig. 10

Fig. 11

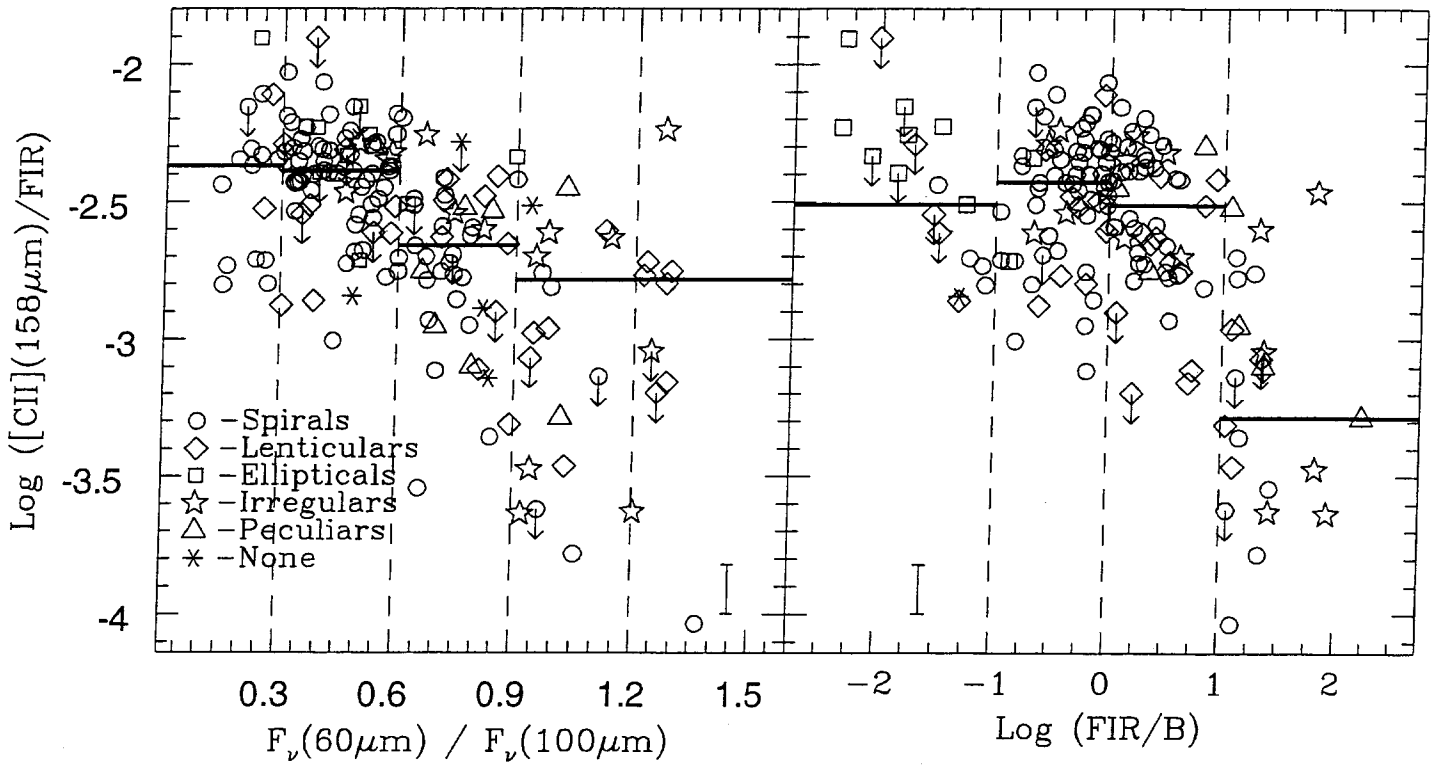
Log ([CII](158μm)/FIR)
-2
-2.5
-3
-3.5
-4
○ –Spirals
◇ –Lenticulars
□ –Ellipticals
☆ –Irregulars
△ –Peculiars
✳ –None
0.3
0.6
0.9
1.2
1.5
F_ν(60μm) / F_ν(100μm)
−2
−1
0
1
2
Log (FIR/B)

Fig. 12

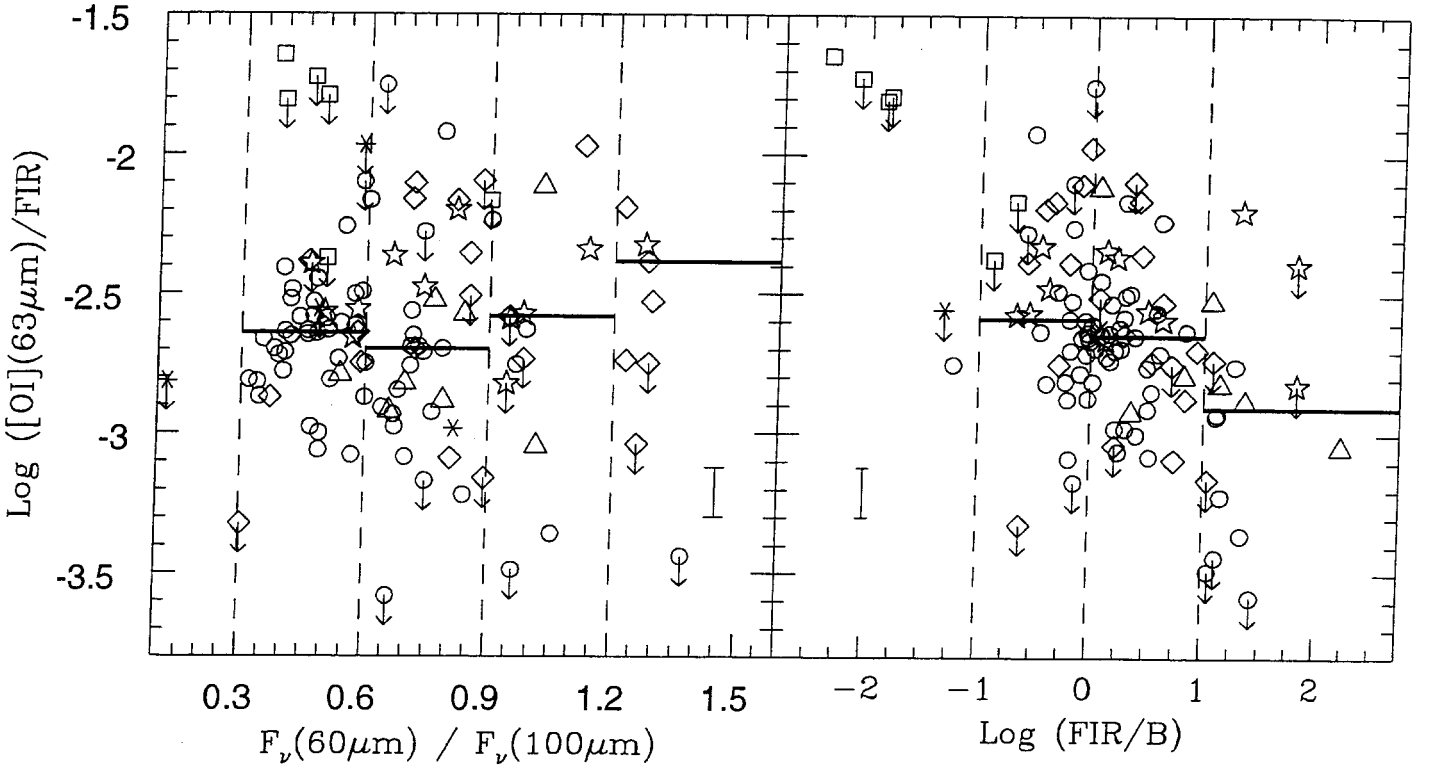
-1.5
-2
-2.5
-3
-3.5
Log ([OI](63μm)/FIR)
0.3
0.6
0.9
1.2
1.5
F_ν(60μm) / F_ν(100μm)
−2
−1
0
1
2
Log (FIR/B)

Fig. 13

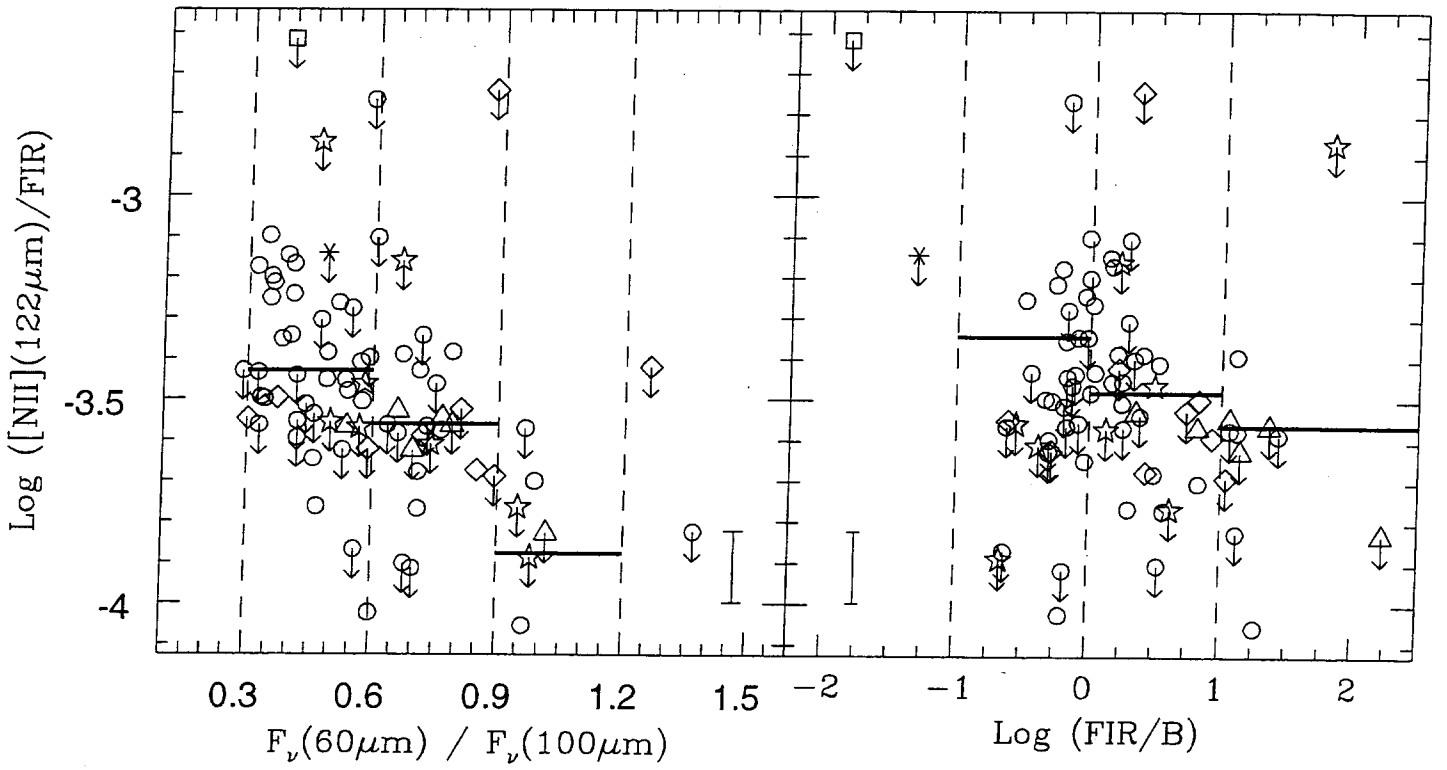
Log ([NII](122μm)/FIR)
-3
-3.5
-4
0.3
0.6
0.9
1.2
1.5
F_ν(60μm) / F_ν(100μm)
−2
−1
0
1
2
Log (FIR/B)

Fig. 14

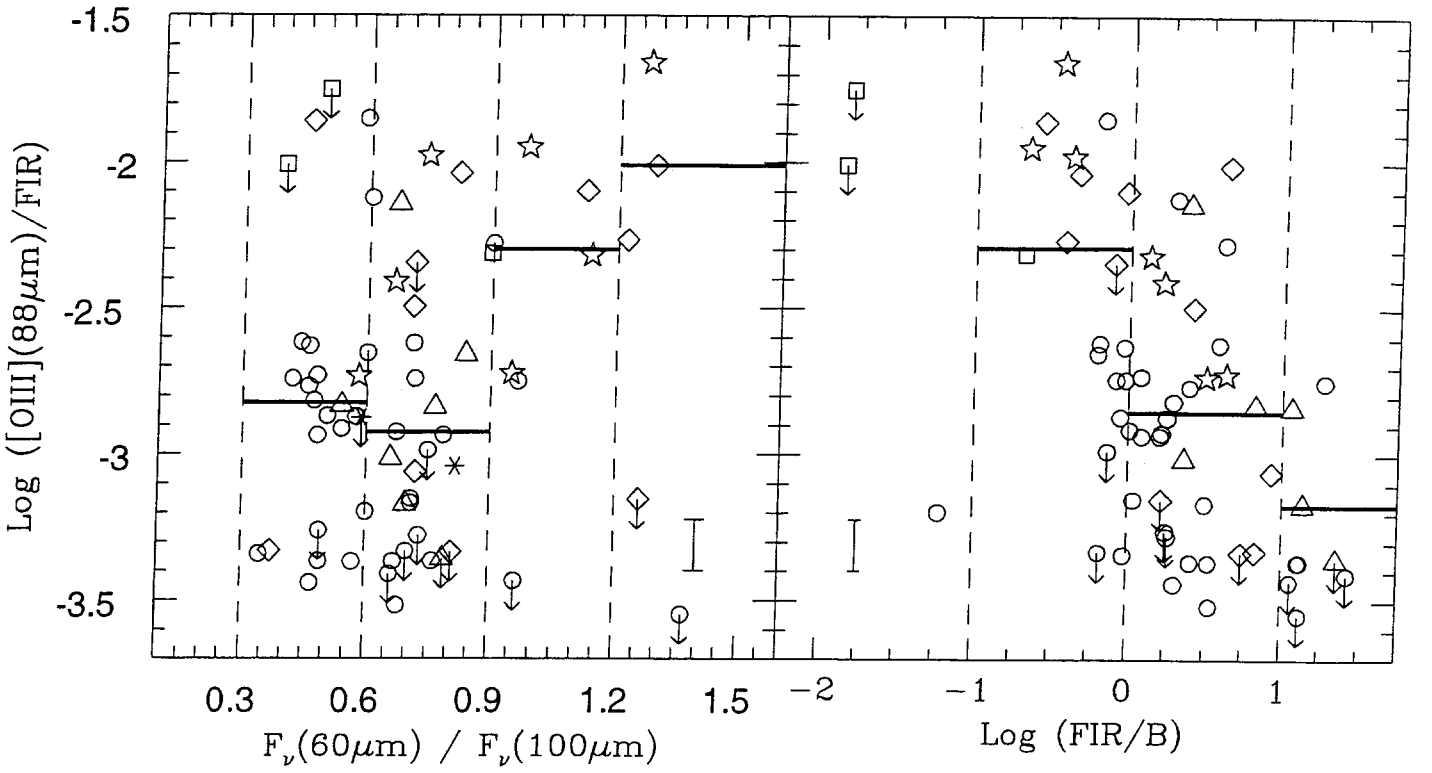
-1.5
-2
-2.5
-3
-3.5
Log ([OIII](88μm)/FIR)
0.3
0.6
0.9
1.2
1.5
F_ν(60μm) / F_ν(100μm)
−2
−1
0
1
Log (FIR/B)

Fig. 15

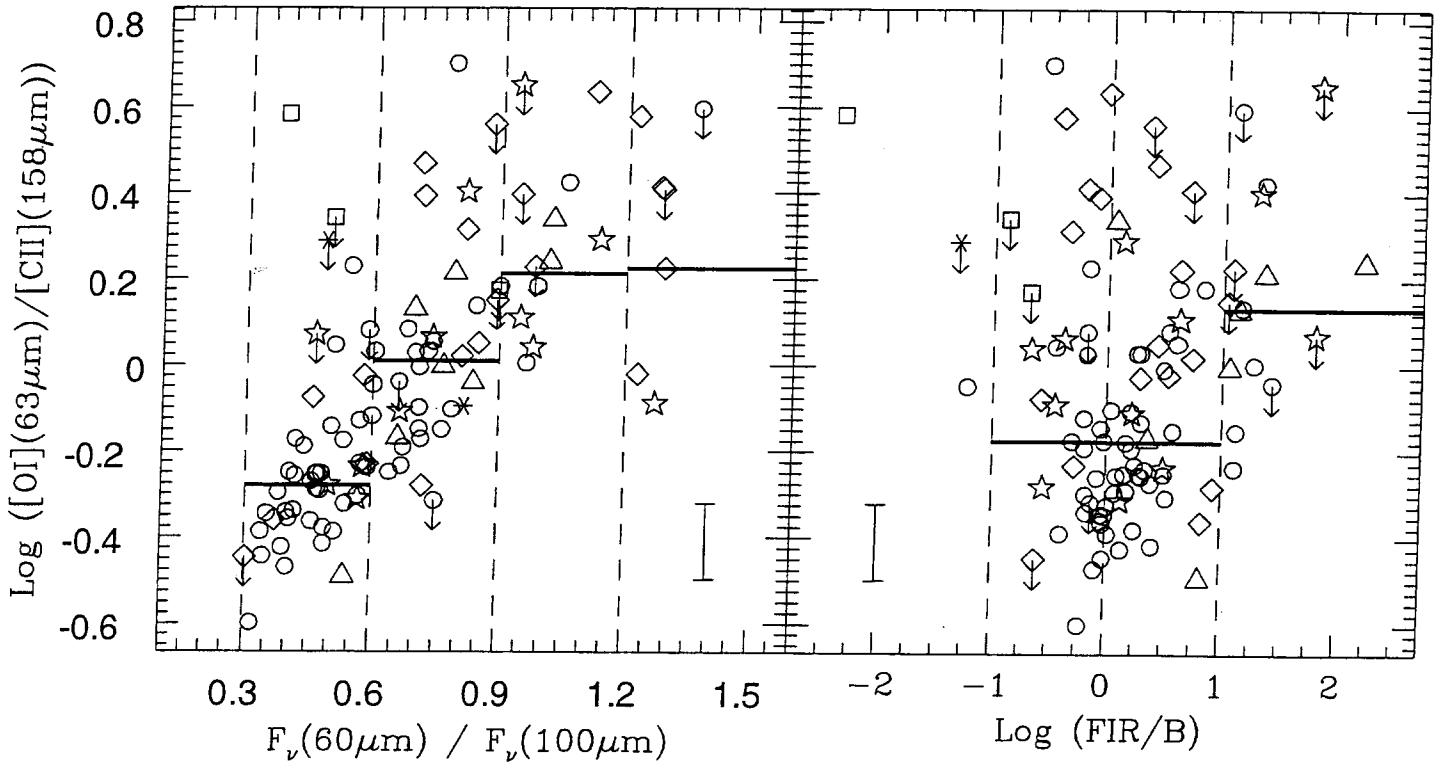
0.8
0.6
0.4
0.2
0
-0.2
-0.4
-0.6
Log ([OI](63μm)/[CII](158μm))
0.3
0.6
0.9
1.2
1.5
F_ν(60μm) / F_ν(100μm)
−2
−1
0
1
2
Log (FIR/B)

Fig. 16

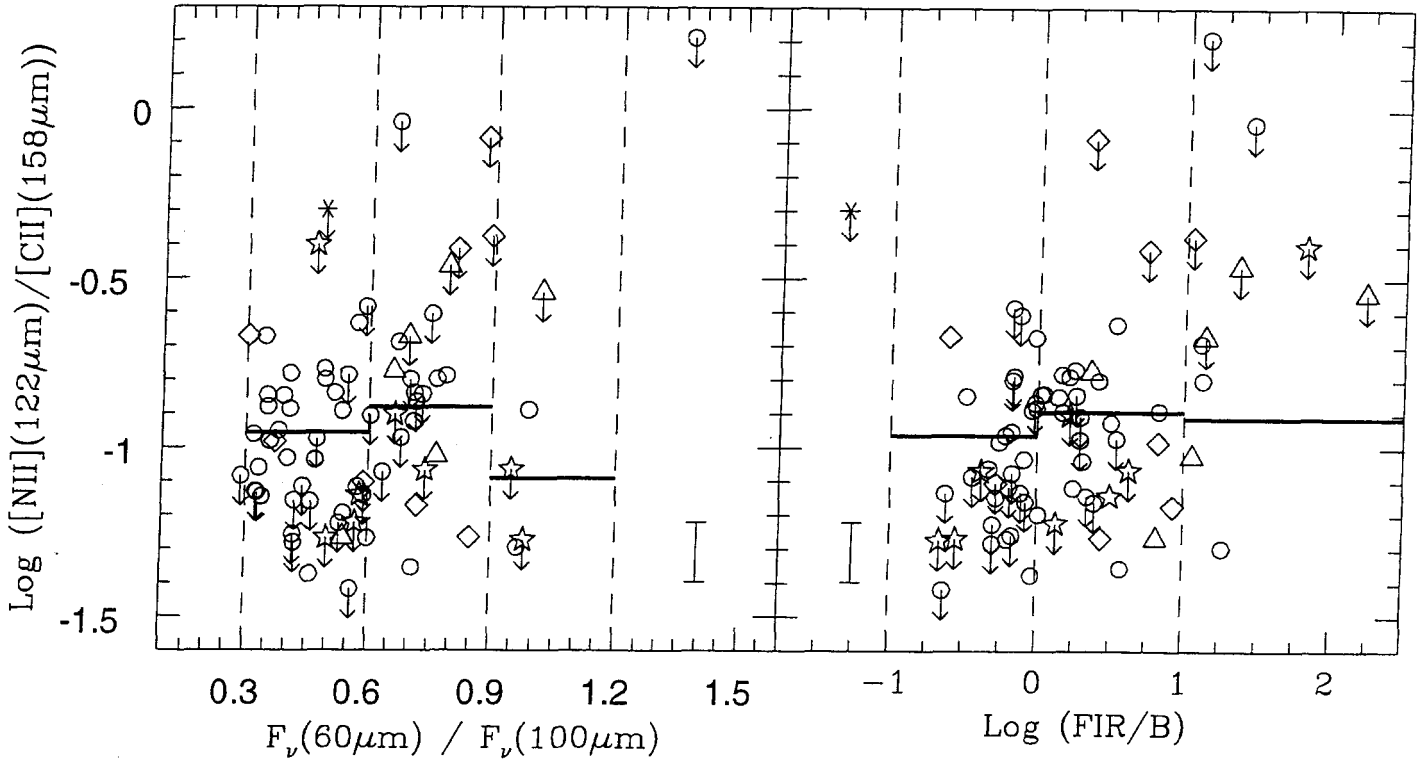
Log ([NII](122μm)/[CII](158μm))
0
-0.5
-1
-1.5
0.3
0.6
0.9
1.2
1.5
F_ν(60μm) / F_ν(100μm)
−1
0
1
2
Log (FIR/B)

Fig. 17

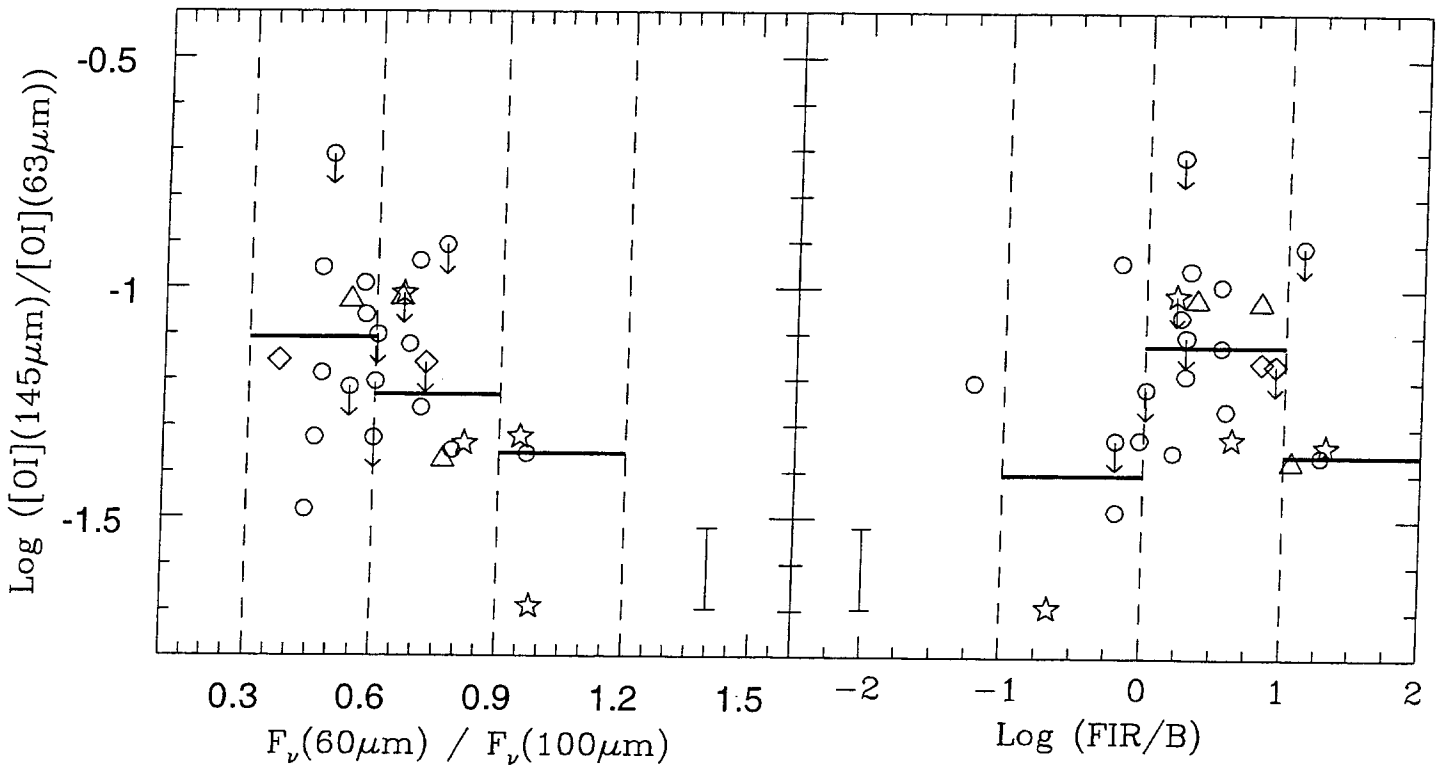
-0.5
-1
-1.5
Log ([OI](145μm)/[OI](63μm))
0.3
0.6
0.9
1.2
1.5
F_ν(60μm) / F_ν(100μm)
−2
−1
0
1
2
Log (FIR/B)

Fig. 18

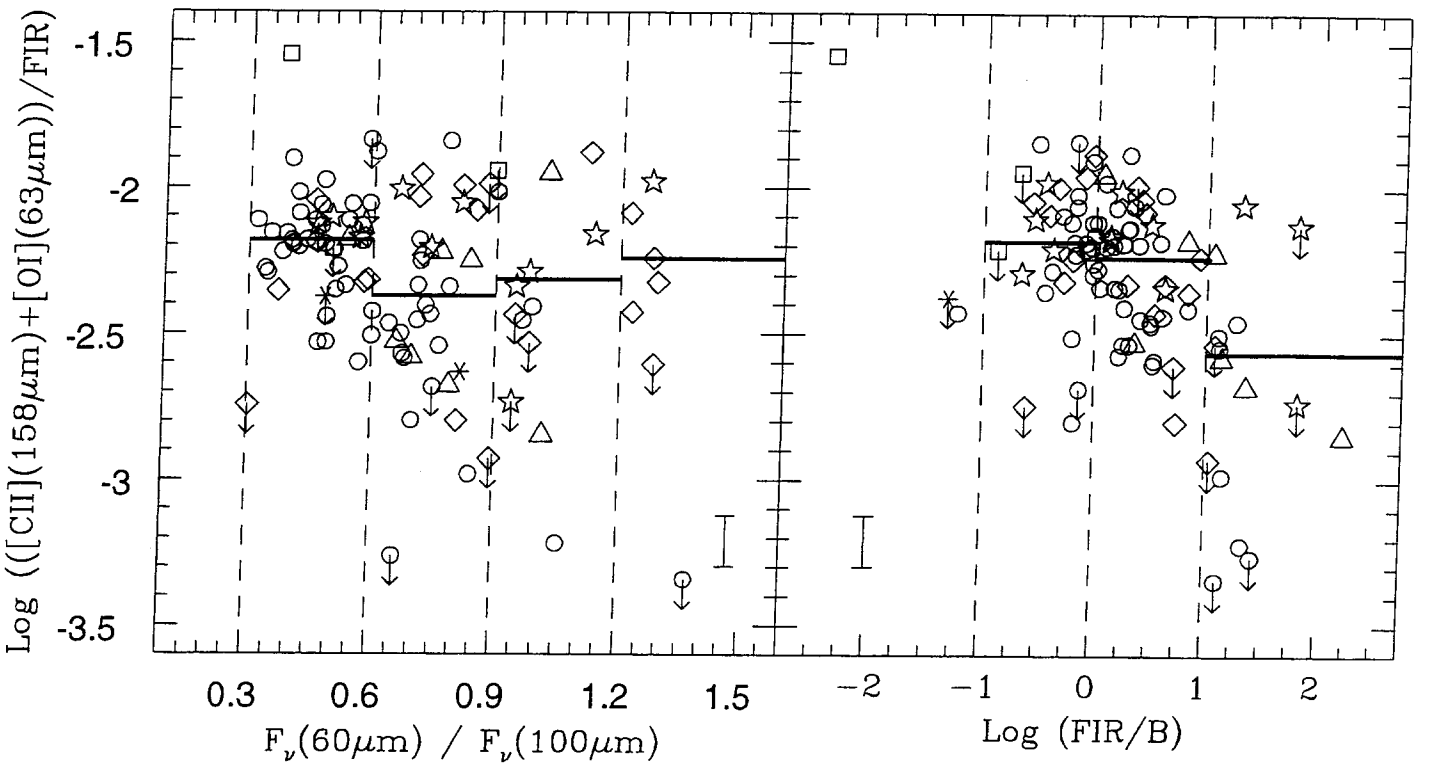
Log (([CII](158μm)+[OI](63μm))/FIR)
-1.5
-2
-2.5
-3
-3.5
0.3
0.6
0.9
1.2
1.5
F_ν(60μm) / F_ν(100μm)
−2
−1
0
1
2
Log (FIR/B)

Fig. 19

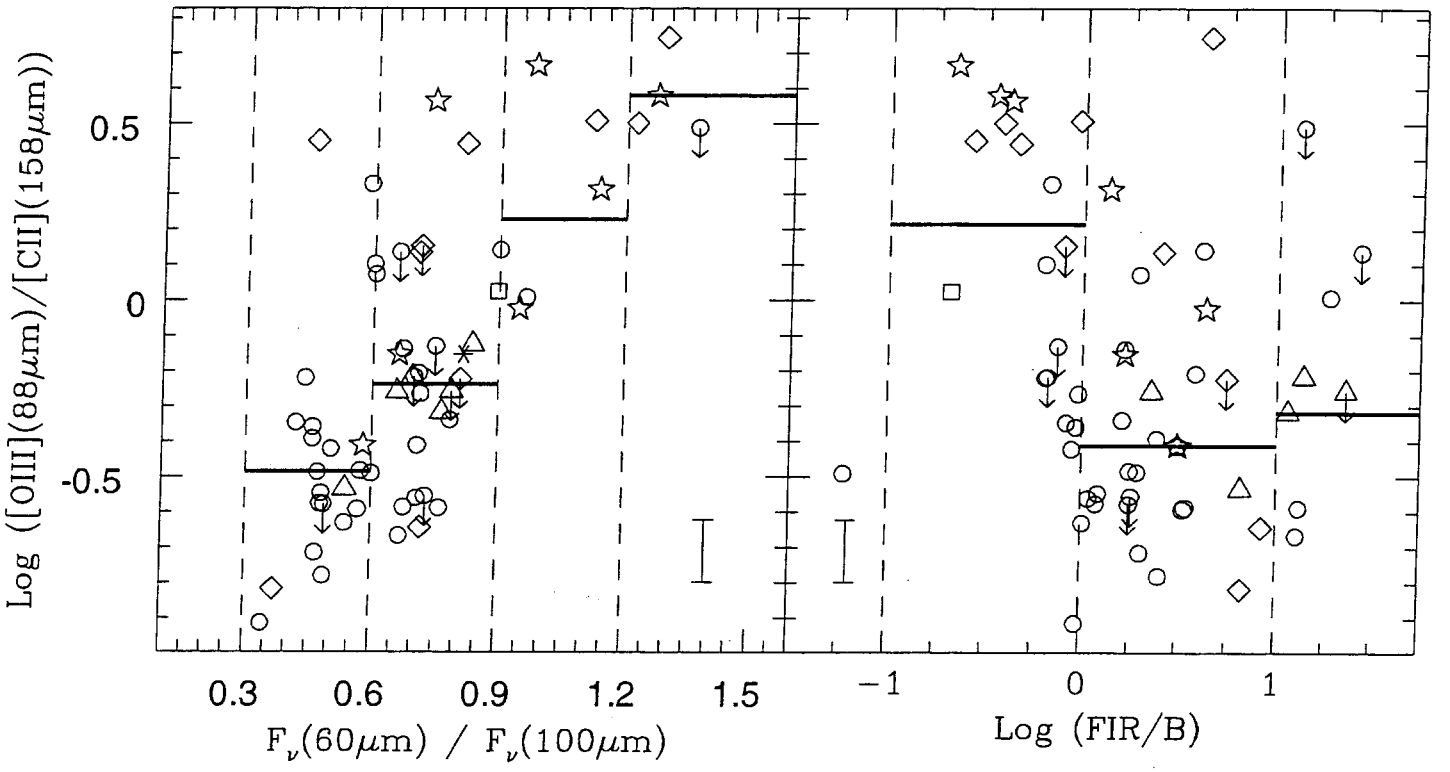
Log ([OIII](88μm)/[CII](158μm))
0.5
0
-0.5
0.3
0.6
0.9
1.2
1.5
$F_\nu(60\mu m)$ / $F_\nu(100\mu m)$
−1
0
1
Log (FIR/B)

Fig. 20

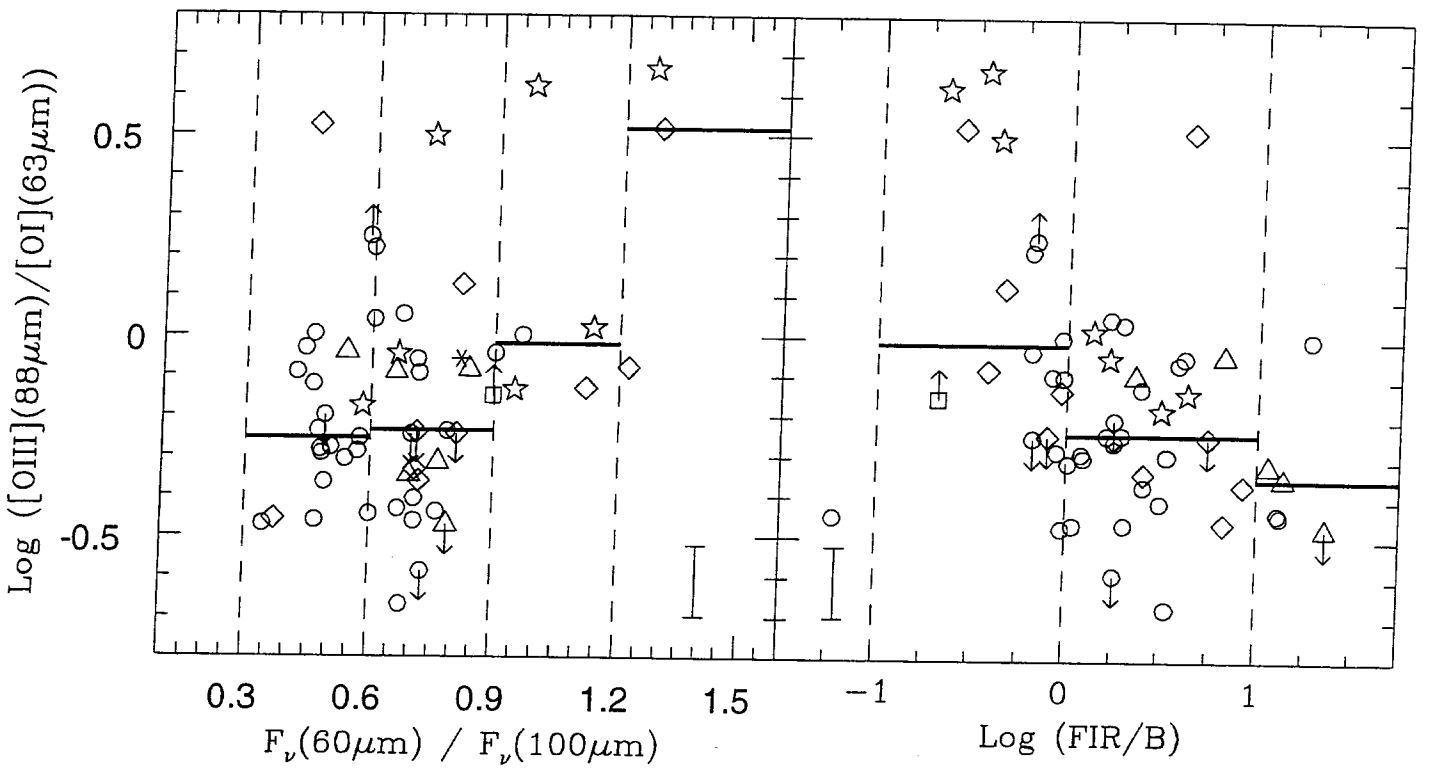
Log ([OIII](88μm)/[OI](63μm))
0.5
0
-0.5
0.3
0.6
0.9
1.2
1.5
$F_\nu(60\mu m)$ / $F_\nu(100\mu m)$
−1
0
1
Log (FIR/B)

Fig. 21

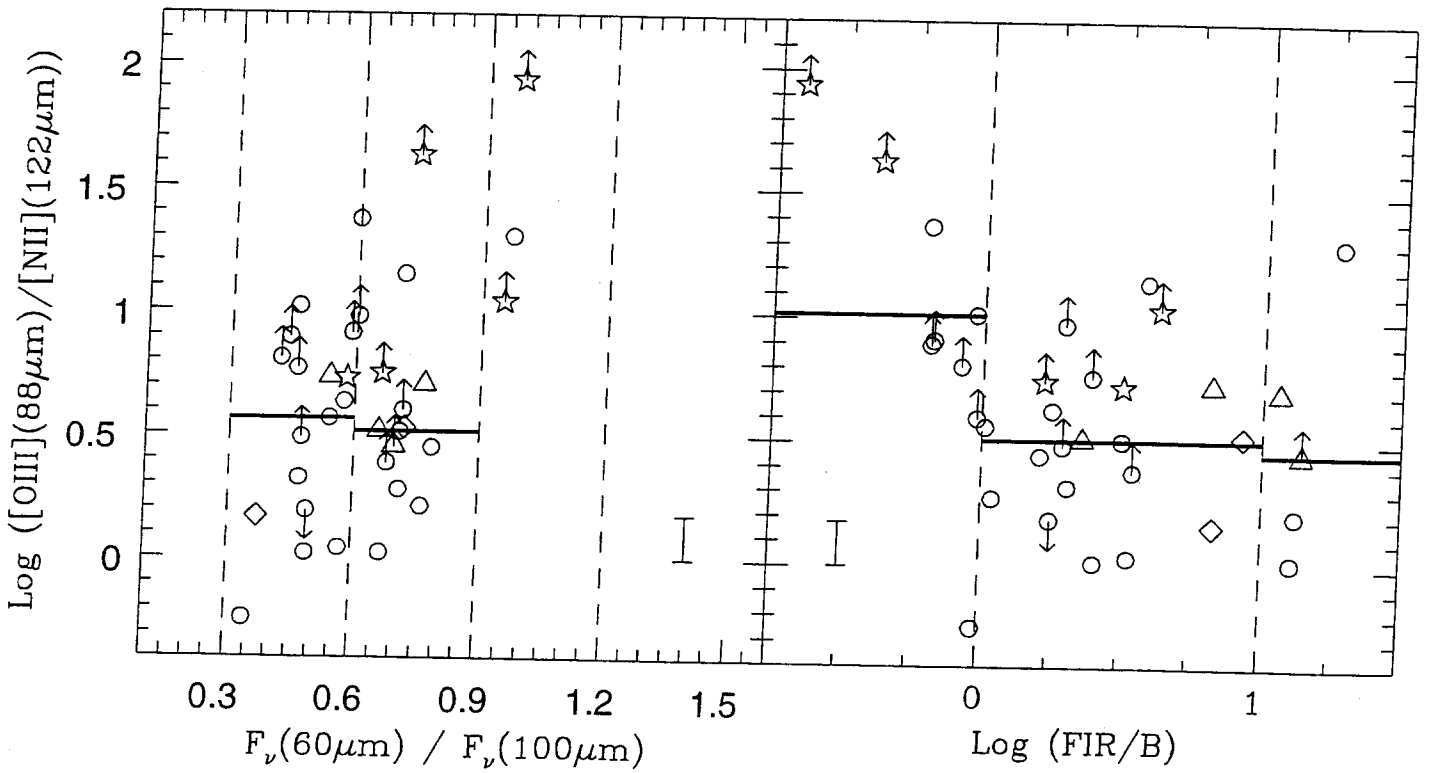
Log ([OIII](88μm)/[NII](122μm))
2
1.5
1
0.5
0
0.3
0.6
0.9
1.2
1.5
$F_\nu(60\mu m)$ / $F_\nu(100\mu m)$
0
1
Log (FIR/B)

Fig. 22

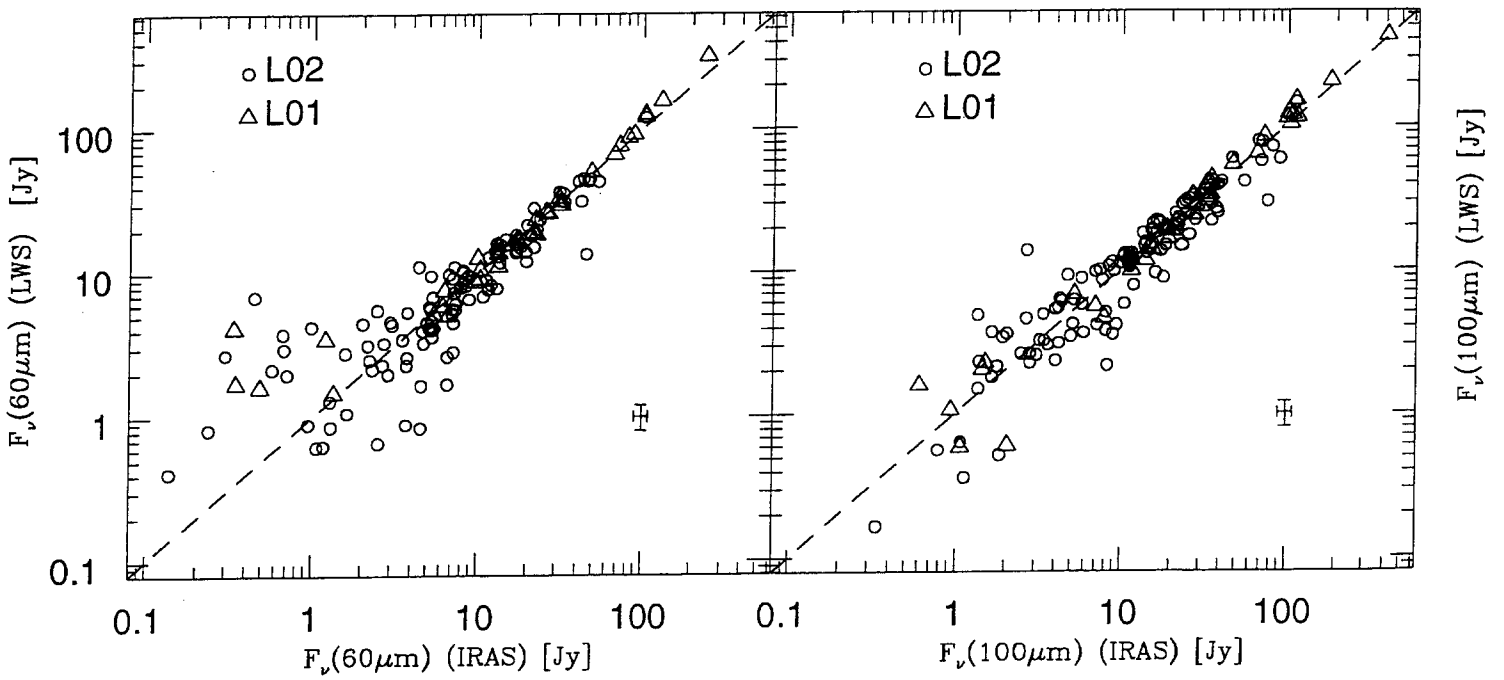
o L02
△ L01
100
10
1
0.1
0.1
1
10
100
F_ν(60μm) (LWS) [Jy]
F_ν(60μm) (IRAS) [Jy]
o L02
△ L01
0.1
1
10
100
F_ν(100μm) (IRAS) [Jy]
F_ν(100μm) (LWS) [Jy]

Fig. 23

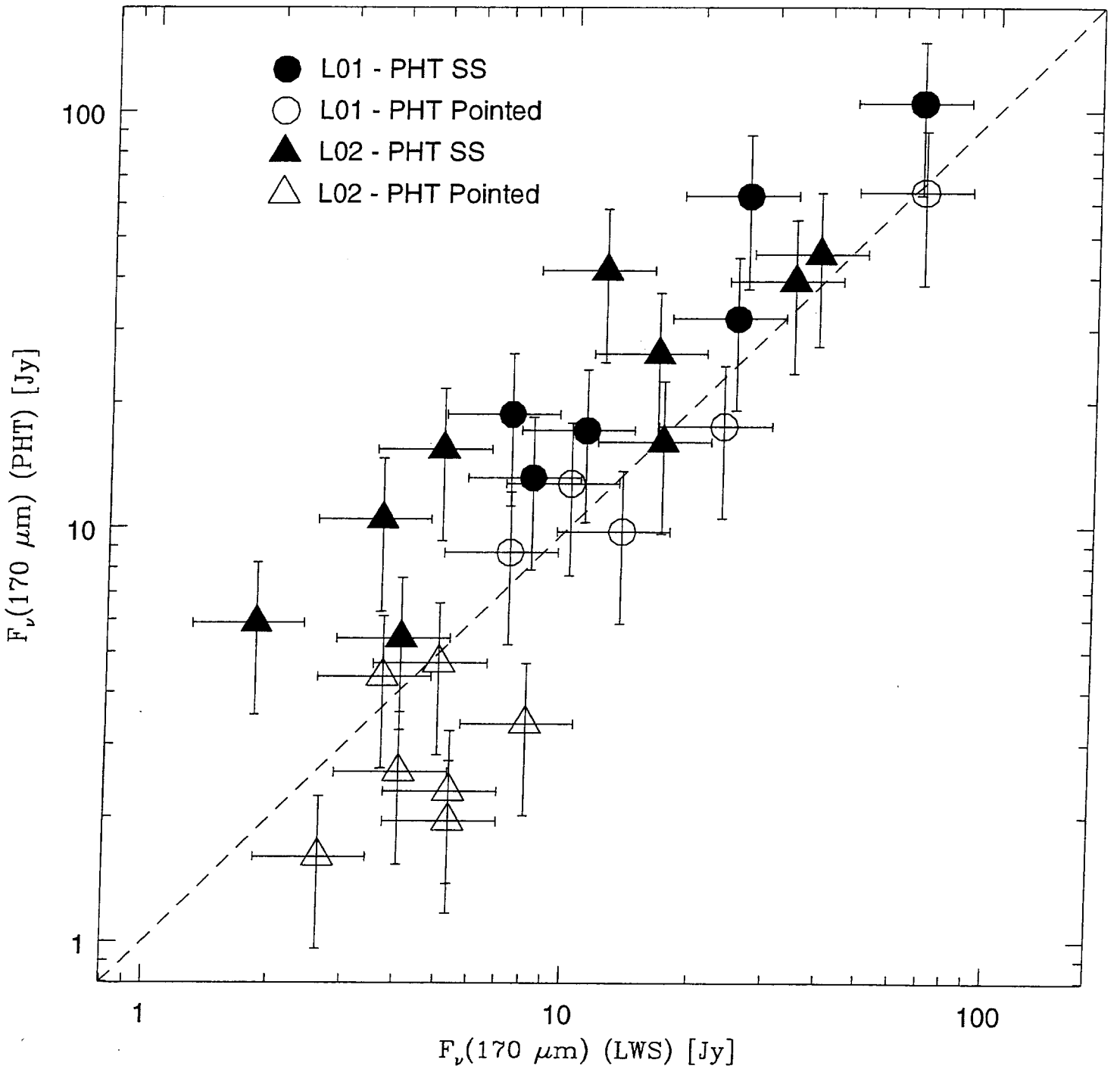
L01 - PHT SS
L01 - PHT Pointed
L02 - PHT SS
L02 - PHT Pointed
100
10
1
1
10
100
F_ν(170 μm) (PHT) [Jy]
F_ν(170 μm) (LWS) [Jy]

Table 1. Galaxies and Properties

Galaxy	RA (J2000)	Dec (J2000)	V (km/s)	RC3[b]	a[c]	b[c]	12um (Jy)	25um (Jy)	60um (Jy)	100um (Jy)	60/100
IC 10[a]	00 20 24.55	+59 17 30.5	-344	10	6.3	5.1	4.88	13.95	112.92	179.24	0.630
ESO 350-IG38	00 36 52.53	-33 33 18.6	6156	-2			0.41	2.49	6.47	5.01	1.291
Cartwheel	00 37 40.80	-33 42 58.0	9050	10	1.1	0.9	0.08	0.11	0.73	1.57	0.464
NGC 185	00 38 57.69	+48 20 12.2	-202	-5	11.7	10	0.04	<0.03	0.35	1.46	0.239
NGC 247[a]	00 47 08.30	-20 45 37.6	160	7	21.4	6.9	<0.12	<0.16	7.93	27.32	0.291
NGC 253[a]	00 47 34.37	-25 17 32.0	245	5	27.5	6.8	55.84	155.65	998.73	1861.67	0.536
NGC 278	00 52 04.58	+47 33 02.0	640	3	2.1	2.0	1.63	2.57	25.05	46.39	0.540
UGC 00545	00 53 34.90	+12 41 36.0	18330	-1	0.5	0.5	0.51	1.21	2.24	2.63	0.851
MCG +12-02-001	00 54 04.01	+73 05 12.6	4706	99			0.76	3.71	22.37	26.68	0.838
NGC 300[a]	00 54 53.72	-37 40 56.9	144	7	21.9	15.5	0.53	0.64	23.08	74.45	0.310
IC 1613[a]	01 05 02.00	+02 08 03.0	-234	10	16.2	14.5	0.08	0.11	0.68	1.78	0.382
NGC 449	01 16 07.23	+33 05 22.3	4780	-1	0.8	0.5	0.34	0.89	2.53	3.05	0.829
UGC 00852	01 19 38.30	+17 33 53.0	8817	5	1.1	0.4	0.14	0.13	0.77	4.02	0.191
NGC 520	01 24 34.90	+03 47 30.0	2266	99	1.9	0.7	0.76	2.84	31.10	47.12	0.660
M 33[a]	01 33 50.90	+30 39 37.0	-179	6	70.8	41.7	32.69	40.26	419.65	1256.43	0.334
NGC 625	01 35 04.20	-41 26 15.0	405	9	5.8	1.9	0.20	0.94	5.09	9.07	0.561
NGC 628[a]	01 36 41.70	+15 46 59.0	657	5	10.5	9.5	2.07	1.9	20.86	65.64	0.317
NGC 660	01 43 01.70	+13 38 34.0	850	1	8.3	3.2	2.31	7.05	67.27	104.89	0.641
Mrk 573	01 43 57.80	+02 21 00.0	5174	-1	1.3	1.3	0.23	0.79	1.11	1.36	0.816
III Zw 35	01 44 30.50	+17 06 08.0	8225	11			0.09	1.08	13.33	14.13	0.943
NGC 685	01 47 43.10	-52 45 40.0	1356	5	3.7	3.3	0.13	0.15	1.60	7.14	0.224
NGC 693	01 50 31.00	+06 08 42.0	1567	90	2.1	1.0	0.29	0.55	6.73	11.81	0.570
NGC 695	01 51 14.20	+22 34 57.0	9735	10	0.8	0.7	0.48	0.86	7.87	13.57	0.58
UGC 01449	01 58 06.70	+03 05 15.0	5589	9	1.2	0.7	0.31	0.56	4.96	8.41	0.59
NGC 821	02 08 21.20	+10 59 41.0	1735	-5	2.6	1.6					
NGC 814	02 10 37.70	-15 46 24.0	1616	-2	1.3	0.5	0.19	1.01	4.41	3.59	1.230
Arp 273	02 21 32.78	+39 21 29.9	7563				<0.17	0.24	1.87	3.85	0.486
NGC 891[a]	02 22 33.04	+42 20 47.7	528	3	13.5	2.5	5.66	7.78	61.10	198.63	0.307
NGC 925[a]	02 27 17.00	+33 34 43.0	553	7	10.5	5.9	0.26	0.66	7.65	26.68	0.286
NGC 986	02 33 34.10	-39 02 41.0	2005	2	3.9	3.0	1.41	3.65	25.14	51.31	0.490
NGC 1022	02 38 32.70	-06 40 40.0	1453	1	2.4	2.0	0.75	3.29	19.83	27.16	0.730
NGC 1052	02 41 04.80	-08 15 20.8	1470	-5	3.0	2.1	0.20	0.49	0.93	1.50	0.620

Table 2. FIR Continuum Fluxes

Galaxy	170μm (Jy)	158μm (Jy)	145μm (Jy)	122μm (Jy)	88μm (Jy)	63μm (Jy)	57μm (Jy)	52μm (Jy)
NGC 185	2.0 (0.5)	1.5 (0.2)	1.6 (0.2)	2.8 (0.3)				
UGC 00545		4.8 (0.5)				5.8 (0.6)		
MCG +12-02-001	27.8 (2.1)	28.9 (3.1)	28.7 (2.3)	30.1 (2.7)	37.4 (4.4)	30.2 (2.8)	24.8 (2.2)	21.8 (2.0)
IC 1613		1.6 (0.2)	1.7 (0.2)			2.2 (0.3)		
NGC 449		4.4 (0.6)	2.9 (0.3)	2.4 (0.3)		5.2 (0.5)	2.4 (1.3)	
UGC 00852	6.3 (4.2)	1.3 (1.0)	3.7 (0.7)	4.3 (0.7)				
NGC 520	29.6 (2.8)	33.0 (4.3)	39.4 (4.2)	48.7 (3.7)	57.7 (7.6)	44.4 (4.6)	37.9 (3.4)	30.7 (2.8)
NGC 625	8.8 (1.6)		3.5 (0.6)	5.9 (1.0)	4.0 (0.6)		5.5 (0.8)	
NGC 660	75.6 (7.6)	92.0 (9.2)	91.5 (9.2)	106.3 (10.6)	110.0 (11.2)	80.3 (8.0)	70.1 (7.1)	60.4 (6.1)
Mrk 573		1.1 (0.2)	1.8 (0.3)	2.0 (0.2)	3.7 (0.5)	8.4 (0.9)		
III Zw 35	12.5 (1.2)	5.3 (0.6)	8.2 (0.8)	10.4 (1.0)	9.9 (1.3)	18.4 (1.7)	16.2 (1.5)	8.5 (1.0)
NGC 685			3.0 (0.5)					
NGC 693		10.7 (2.3)	7.6 (1.0)	11.0 (0.9)		14.5 (1.5)		
NGC 695	15.5 (1.4)		18.5 (1.5)	14.9 (1.3)	19.3 (2.4)	12.6 (1.2)		
UGC 01449	7.4 (1.2)	6.9 (1.6)	6.9 (0.7)	8.1 (0.7)		8.2 (0.9)		
NGC 814	1.3 (0.2)	4.1 (1.0)		4.2 (0.3)		14.6 (1.5)		
NGC 986	28.2 (2.5)	39.8 (5.8)	37.0 (3.4)	46.4 (3.0)	44.1 (5.5)	26.1 (2.7)	25.6 (2.2)	23.0 (2.1)
NGC 1022	22.5 (2.0)	24.0 (3.3)	21.0 (2.4)	26.0 (2.4)	36.7 (4.3)	27.1 (2.5)	24.6 (2.3)	23.3 (2.0)
UGC 02238	18.8 (1.8)	23.8 (2.9)	18.4 (1.9)	17.2 (1.4)	24.4 (2.4)	17.3 (1.8)	7.4 (1.4)	
NGC 1155		2.6 (0.5)	2.4 (0.3)	2.2 (0.2)		4.1 (0.4)		
NGC 1156	5.3 (0.5)	17.0 (2.1)	7.4 (0.7)	8.2 (0.7)		2.1 (0.2)		
NGC 1222	8.0 (0.9)	10.8 (2.2)	11.4 (1.1)	12.9 (1.1)		20.4 (2.0)	20.2 (1.8)	
UGC 02519	5.5 (0.9)	8.1 (1.8)	7.9 (0.8)	7.7 (0.7)		6.3 (0.6)		
NGC 1266	10.1 (1.0)	14.8 (4.8)	13.3 (1.3)	16.7 (1.3)	21.6 (2.7)	18.5 (1.8)	15.5 (1.4)	
NGC 1275	4.5 (0.6)	7.8 (0.9)	7.5 (0.8)	6.4 (0.5)	7.3 (1.0)	12.1 (1.2)	10.7 (1.0)	11.5 (1.2)
NGC 1317	2.6 (0.3)	7.5 (1.5)				5.1 (0.5)		
NGC 1326	10.3 (1.0)			13.6 (1.0)		13.0 (1.2)		
IC 1953	2.0 (0.3)	8.4 (1.0)		7.3 (0.6)	13.2 (1.6)	11.5 (1.2)		
NGC 1377		5.8 (0.8)		4.2 (0.4)	11.3 (1.3)	13.6 (1.3)		
NGC 1385	20.2 (1.7)	23.3 (4.3)	26.8 (3.0)	27.9 (2.2)	28.9 (3.5)	23.7 (2.2)	19.9 (1.6)	
UGC 02855	66.8 (5.7)	67.3 (8.9)	57.6 (4.6)	64.2 (4.9)	59.4 (7.6)	37.8 (3.7)	22.2 (1.9)	17.7 (1.6)
NGC 1482	55.7 (4.8)		50.5 (4.1)	52.7 (4.5)	61.7 (7.4)	40.7 (4.1)	37.3 (3.2)	30.4 (2.6)

Table 3. Detected Far-Infrared Lines

Line	Wavelength (μm)	Transition
[OIII]	51.82	$^3P_2 \rightarrow {}^3P_1$
OH[a]	52.93/53.06	$(^2\pi_{3/2})$ J=11/2 → $(^2\pi_{3/2})$ J=9/2
	53.26/53.35	$(^2\pi_{1/2})$ J=3/2 → $(^2\pi_{3/2})$ J=3/2
[NIII]	57.32	$^2P_{3/2} \rightarrow {}^2P_{1/2}$
H_2O	58.70	o-H_2O 4_{32}-3_{21}
[OI]	63.18	$^3P_1 \rightarrow {}^3P_2$
OH[a]	65.13/65.28	$(^2\pi_{3/2})$ J=9/2 → $(^2\pi_{3/2})$ J=7/2
H_2O[a]	66.44	o-H_2O 3_{30}-2_{21}
	67.09	p-H_2O 3_{31}-2_{20}
Unidentified Line	74.24	
H_2O	75.38	o-H_2O 3_{21}-2_{12}
OH[a]	79.12/79.18	$(^2\pi_{1/2})$ J=1/2 → $(^2\pi_{3/2})$ J=3/2
OH[a]	84.42/84.60	$(^2\pi_{3/2})$ J=7/2 → $(^2\pi_{3/2})$ J=5/2
[OIII]	88.36	$^3P_1 \rightarrow {}^3P_0$
H_2O[a]	100.91	o-H_2O 5_{14}-4_{23}
	100.98	p-H_2O 2_{20}-1_{11}
H_2O	108.07	o-H_2O 2_{21}-1_{10}
OH[a]	119.23/119.44	$(^2\pi_{3/2})$ J=5/2 → $(^2\pi_{3/2})$ J=3/2
[NII]	121.89	$^3P_2 \rightarrow {}^3P_1$
[OI]	145.53	$^3P_0 \rightarrow {}^3P_1$
[CII]	157.71	$^2P_{3/2} \rightarrow {}^2P^1_{/2}$
OH[a]	163.12/163.40	$(^2\pi_{1/2})$ J=3/2 → $(^2\pi_{1/2})$ J=1/2
CO[a]	162.81	CO J=16→15

[a] Line detected cannot be accurately identified due to the resolution of the LWS. The line is one or a blend of the listed transitions.

Table 4. FIR Emission Line Fluxes

Galaxy	TDT[a]	AOT[b]	RA (J2000)	Dec (J2000)	158μm[c]	145μm[c]	122μm[c]	88μm[c]	63μm[c]	57μm[c]	52μm[c]
IC 10	45700606[d]	L02	00 19 37.6	+59 23 31	2.15 (0.05)				0.53 (0.06)		
IC 10	45700607[d]	L02	00 21 11.5	+59 11 30	1.29 (0.05)						
IC 10	45700608[d]	L02	00 20 14.0	+59 18 38	3.64 (0.14)		0.38 (0.08)	10.56 (0.35)	3.33 (0.34)		
IC 10	45700609[d]	L02	00 20 25.3	+59 17 17	7.63 (0.21)	0.24 (0.04)	0.46 (0.11)	15.97 (0.57)	6.57 (0.20)	<3.51	11.86 (0.94)
IC 10	45700610[d]	L02	00 19 58.3	+59 17 02	2.01 (0.07)				1.32 (0.07)		
ESO 350 IG38	54900720	L02	00 36 52.8	-33 33 23	0.48 (0.04)			2.67 (0.30)	0.81 (0.09)		
Cartwheel	37101917	L02	00 37 40.1	-33 43 26	0.15 (0.02)		<0.06		<0.18		
NGC 185	78500682	L01	00 38 56.9	+48 20 10	0.37 (0.10)						
NGC 247	57001101[d]	L02	00 47 06.5	-20 41 07	<0.21						
NGC 247	57001101[d]	L02	00 47 06.9	-20 42 06	0.16 (0.03)						
NGC 247	57001101[d]	L02	00 47 07.3	-20 43 06	0.53 (0.08)						
NGC 247	57001101[d]	L02	00 47 07.8	-20 44 05	0.43 (0.04)						
NGC 247	57001101[d]	L02	00 47 08.2	-20 45 05	0.47 (0.06)						
NGC 247	57001101[d]	L02	00 47 08.7	-20 46 05	0.51 (0.03)						
NGC 247	57001101[d]	L02	00 47 09.1	-20 47 04	0.41 (0.05)						
NGC 247	57001101[d]	L02	00 47 09.6	-20 48 04	0.49 (0.12)						
NGC 247	57001101[d]	L02	00 47 10.0	-20 49 04	0.29 (0.04)						
NGC 247	57001101[d]	L02	00 47 10.4	-20 50 04	0.15 (0.04)						
NGC 253	24701103[d]	L01	00 47 33.3	-25 17 18	48.93 (0.86)	2.94 (0.52)	7.28 (0.77)	8.38 (1.27)	38.83 (1.47)		
NGC 253	24701145[d]	L02	00 47 28.2	-25 18 15	11.41 (0.17)	<0.89	2.18 (0.24)	<2.27	4.26 (0.25)		
NGC 253	24701145[d]	L02	00 47 38.3	-25 16 20	12.11 (0.33)	<0.61	1.94 (0.39)	<1.69	5.07 (0.38)		
NGC 253	56901708[d]	L01	00 47 33.3	-25 17 18	50.53 (0.66)		8.23 (0.71)		38.43 (0.92)		
NGC 253	79900107[d]	L02	00 47 33.2	-25 17 16		3.82 (0.28)	9.11 (0.72)				
NGC 253	79900210[d]	L02	00 47 33.2	-25 17 16					42.49 (1.27)		
NGC 253	79900309[d]	L02	00 47 33.2	-25 17 17				9.06 (0.87)			
NGC 278	59702260	L02	00 52 04.6	+47 33 01	7.28 (0.12)	<0.21	0.46 (0.06)	1.71 (0.18)	3.47 (0.16)	<1.07	1.19 (0.33)
UGC 00545	57701507	L02	00 53 34.9	+12 41 36	<0.13				<0.33		
UGC 00545	57701507	L02	00 53 34.9	+12 44 36	<0.16				<0.40		
MCG +12-02-001	47300813	L01	00 54 03.8	+73 05 03	3.11 (0.11)			2.34 (0.24)	2.84 (0.27)		
NGC 300	54901001[d]	L02	00 54 28.5	-37 39 01	0.20 (0.02)						
NGC 300	54901001[d]	L02	00 54 34.8	-37 39 30	0.40 (0.04)						
NGC 300	54901001[d]	L02	00 54 41.1	-37 39 59	0.57 (0.02)						
NGC 300	54901001[d]	L02	00 54 47.4	-37 40 28	0.70 (0.03)						
NGC 300	54901001[d]	L02	00 54 53.7	-37 40 56	0.48 (0.04)						
NGC 300	54901051[d]	L01	00 54 28.5	-37 39 01	<0.24				<1.14		
NGC 300	54901051[d]	L01	00 54 34.8	-37 39 30	0.44 (0.07)				<0.91		
NGC 300	54901051[d]	L01	00 54 41.1	-37 39 59	0.53 (0.05)				<1.12		
NGC 300	54901051[d]	L01	00 54 47.4	-37 40 28	0.68 (0.07)				<1.02		
NGC 300	54901051[d]	L01	00 54 53.7	-37 40 57	0.57 (0.07)				<1.20		
NGC 300	54901103[d]	L02	00 54 57.6	-37 42 40	0.28 (0.04)						
NGC 300	54901103[d]	L02	00 55 03.8	-37 43 08	0.85 (0.03)						

Table 5. Molecular and Unidentified Line Fluxes

Galaxy	TDT[a]	RA	Dec	53μm[b]	59μm[b]	65μm[b]	67μm[b]	74μm[b,f]	75μm[b]	79μm[b]	84μm[b]	101μm[b]	108μm[b]	119μm[b]	163μm[b]
NGC 253	24701103[c]	00 47 33.3	-25 17 18											11.76[e]	
NGC 253	56901708[c]	00 47 33.3	-25 17 18	7.12[e]										11.63[e]	
NGC 253	79900508[c]	00 47 33.3	-25 17 18												2.24[d]
NGC 891	61100256[c]	02 22 33.0	+42 20 55											1.11[e]	
NGC 891	61401144[c]	02 22 33.2	+42 20 58											1.33[e]	
NGC 1068	82000605	02 42 40.6	-00 00 48							1.36[d]					
NGC 1068	82000704	02 42 40.6	-00 00 48					1.32[d]						1.31[d]	
NGC 1068	82001106	02 42 40.6	-00 00 48					1.24[d]						1.60[d]	
M 82	18000501[c]	09 55 52.4	+69 40 46											7.88[e]	
M 82	65800502[c]	09 55 52.2	+69 40 46											8.17[e]	
M 82	65800611[c]	09 55 52.2	+69 40 46											8.45[e]	
Mrk 231	05100540	12 56 14.6	+56 52 24								1.10[e]				
Mrk 231	18001306	12 56 14.2	+56 52 24								1.09[e]			0.31[e]	
Mrk 231	60300241	12 56 14.2	+56 52 24								0.65[e]			0.34[e]	
NGC 4945	08101705[c]	13 05 26.2	-49 28 15											13.15[e]	
NGC 4945	28000440[c]	13 05 26.5	-49 27 54									7.44[e]		11.62[e]	
Arp 220	27800202	15 34 57.2	+23 30 11	4.30[e]		1.85[e]				1.40[e]	3.09[e]	2.01[e]		2.75[e]	0.38[d]
Arp 220	61001559	15 34 57.2	+23 30 11		0.68[e]								0.76[e]		0.40[d]
Arp 220	64000801	15 34 57.2	+23 30 11	5.31[e]		2.10[e]	1.37[e]		1.68[e]		2.34[e]			2.29[e]	
Arp 220	64000916	15 34 57.2	+23 30 11	4.62[e]		1.55[e]	1.36[e]			1.00[e]	2.97[e]			2.84[e]	0.40[d]

Note– Units of right ascension are hours, minutes, and seconds, and units of declination are degrees, arcminutes, and arcseconds of the LWS observation.

[a] TDT = ISO observation number. It has the form RRRSSSOO where RRR=revolution number, SSS=sequence number within the revolution, and OO=observation number within an observer's proposal.

[b] Line fluxes are in units of 10^{-15} W m^{-2}.

[c] Observation considered an extended source in this paper. May require an extended source correction.

[d] Line flux measured in emission

[e] Line flux measured in absorption.

[f] Unidentified line at 74.20μm is included in this table.

Table 6. Serendipitous Galactic [CII] 158μm Detections

Galaxy[a]	TDT[b]	l	b	V (km/s)	158μm (COBE)[c]	(0.5%) FIR[c]	158um (MW)[c,d]	158μm (gal)[c,e]	% Cont[g]
IC 10	45700606	118.89	-3.23	-344	25.38	4.15	20.73 (0.48)	70.93[h]	23.4
	45700607	119.06	-3.45		23.76		12.44 (0.48)		
Maffei 2	85800683[f]	136.48	-0.55	-17	148.97	6.38	27.47 (0.87)	112.62	24.4
NGC 1156	65300185	156.37	-29.28	375	2.92	0.82	2.51 (0.58)	17.54	14.3
UGC 02855	62902697	136.91	+12.33	1202	6.70	1.24	4.85 (0.58)	50.51	9.6
NGC 1569	64600490	143.61	+11.31	-104	7.29	1.38	8.22 (0.86)	65.99	12.5
3C 120	80901988	190.37	-27.40	9896	3.11	0.95	3.95 (0.29)	3.66	0.0
NGC 1614	85501010	204.45	-34.38	4778	2.53	0.35	4.44 (0.39)	21.80	0.0
NGC 3620	27600982	297.19	-14.32	1680	5.78	0.99	3.47 (0.39)	20.93	0.0
UGCA 332	25700705	310.84	+50.49	2107	1.85	0.34	0.87 (0.10)	0.66	0.0
ESO 173-G015	30601434	307.77	+5.04	3006	16.28	6.97	21.80 (2.22)	48.70	0.0
NGC 6821	31900733	32.89	-14.83	1525	5.59	1.06	3.49 (0.58)	9.43	0.0
NGC 6946	45100131	95.80	+12.14	48	6.80	1.25	2.69 (0.49)	20.58[h]	13.1

Note.--Units of l and b are degrees.

[a] Galaxy here refers to the galaxy that was observed when serendipitous Galactic [CII] 158μm was measured.

[b] TDT = ISO observation number. It has the form RRRSSSOO where RRR=revolution number, SSS=sequence number within the revolution, and OO=observation number within an observer's proposal.

[c] [CII] 158μm intensity units are 10^{-6} ergs cm^{-2} s^{-1} sr^{-1}. ISO observations assume a 75" aperture.

[d] Milky Way [CII] 158μm.

[e] [CII] 158μm of external galaxy observed during observation.

[f] Observation considered an extended source in this paper. May require an extended source correction.

[g] Percent of Milky Way [CII] to total [CII] in LWS aperture. This foreground contamination has been removed from the [CII] fluxes listed in Table 4 for these galaxies.

[h] An average value measured in the LWS aperture from multiple observations.

Table 7. Extended Source Corrections

Detector	Aperture Radius (")	Correction[a]
SW1	39	0.88
SW2	42	0.88
SW3	43	0.84
SW4	41	0.73
SW5	40	0.70
LW1	38	0.69
LW2	39	0.69
LW3	35	0.62
LW4	34	0.55
LW5	33	0.48

[a] The fluxes listed in Tables 3 and 4 for extended sources are based on a point source calibration. The multiplicative correction listed here may need to be applied to these fluxes.